Tampere University

Sara M. Toxqui Rodriguez

HYBRID INTEGRATION OF CHALCOGENIDES AND SILICON METAMATERIALS FOR THE MID-IR

Master's thesis
Faculty of Engineering and Natural Sciences
Supervised by Tapio Niemi
October 2023

Abstract

Sara M. Toxqui Rodriguez: HYBRID INTEGRATION OF CHALCOGENIDES AND SILICON METAMATERIALS FOR THE MID-IR
Master's thesis
Tampere University
Master's Degree Programme in Photonics Technologies
2023

Mid-infrared (mid-IR) photonics has become a key technology for numerous applications, such as biochemical sensing and free space optical communications. Photonic integrated circuits (PICs) offer an attractive approach to reduce size, weight, power consumption, and cost of the systems used in these applications.

Silicon photonics (SiP) stands as the preferred PIC platform. Nevertheless, it does not fully address the requirements of emerging applications due to silicon's indirect bandgap, which prevents efficient light emission. Integrating light sources on SiP remains a persistent challenge. Nonetheless, significant efforts have been made, such as the integration of quantum cascade lasers or the generation of nonlinear sources on silicon. However, these approaches often involve complex deposition processes or require high-power pump sources. A promising new alternative is the integration of silicon photonics metamaterials and rare-earth-doped chalcogenides for mid-IR sources.

Here, we present preliminary studies on the design of silicon metamaterial waveguides tailored for mid-infrared (Mid-IR) operation using sub-wavelength gratings. To overcome SOI limitations due to silica absorption and fully utilize the transparency window of silicon ($1 - 8$ μm), we employed suspended silicon platforms.

Finite Difference Method (FDM) and 3D Finite Difference Time Domain (FDTD) simulations using Lumerical software were performed to extract the main relationships between geometrical parameters and properties of the waveguide, such as the effective refractive index, dispersion, and mode effective area.

We report the experimental characterization of SWG-cladded waveguides fabricated with E-beam lithography in a 700 nm silicon on insulator wafer. The samples were characterized in a wavelength range between 5 and 9 μm. Transmission spectra were obtained for all the systems, with a decrease in transmission observed at 7 μm due to silicon absorption.

We have also demonstrated the generation of a supercontinuum in an ideal suspended silicon waveguide, featuring core width of 3.0 μm and duty cycle of 0.43, leading to a small spectrum broadening effect between wavelengths of 2.5 and 4.5 μm.

This work marks a significant step in the study and development of metamaterial suspended silicon structures for mid-IR.

Keywords: mid-IR, silicon photonics, subwavelength regime, suspended waveguides, metamaterial cladding

The originality of this thesis has been checked using the Turnitin Originality Check service.

Preface

In the summer of 2022, I was first formally introduced to the world of silicon photonics and subwavelength structures through the study of multimode interference couplers. I was amazed by the ability to shape material properties and extend the operational bandwidth of the device. It was an experience that piqued my curiosity and opened me to a world of possibilities in photonics and nanotechnology.

Several months later, I had the incredible opportunity to start a new project with Carlos in the Minaphot group : the design of a metamaterial suspended structures capable to operate in the mid-infrared. This project allowed me to further develop myself in this field, learn, push my boundaries, and prepare for the future challenges that await during my PhD studies

First and foremost, I would like to express my gratitude to my supervisors, Carlos Ramos and Tapio Niemi, for their continuous support, feedback, and encouragement at all the stages of my research project. Without them this work would have not been possible. Additionally, I would like to thank the Minaphot team for all their support and help during my internship, especially during the laboratory work.

I am deeply thankful to my family for their love and support, for always encouraging me to push myself and to pursue my dreams even if it means being thousands of kilometres away. Special thanks go to Isaac, Eliana, and Ale for their constant encouragement and great support. Finally, thanks to all my friends and individuals who have made this master an incredible experience.

Sara M. Toxqui
5 October 2023

Contents

1 Introduction

Mid-infrared (mid-IR) photonics has become a key technology for numerous applications, including free space optical communications, thermal imaging, biochemical sensing, long-range LIDAR and environmental monitoring. Hence, there is a growing interest on the development of on-chip broadband mid-IR sources.

The initial section of this chapter is dedicated to introducing the motivation behind the development of on-chip mid-IR laser sources and outlining the objectives of the master's thesis. The second section provides an outline of the manuscript's structure. Finally, the third section comprises an overview of the latest advancements in various mid-infrared platforms and light sources.

1.1 Motivation and objectives

The mid-infrared (mid-IR) wavelength range, spanning from 2 to 20 μm, holds great interest as it host both atmospheric transparency windows (3 – 5 μm and 8 – 13 μm) and covers the distinctive spectral signals of many molecules, including hydrocarbons, carbon monoxide and carbon dioxide.

Mid-infrared (mid-IR) photonics is used in multiple applications, from free space optical communications to environmental monitoring. However, the systems used in these applications generally consist of discrete components such as lasers, modulators, and detectors packaged in rack-size modules. Photonic integrated circuits (PIC) offer an attractive solution to reduce size, weight, power consumption and cost of such systems.

Silicon photonics (SiP) is the preferred platform for PIC development due to its compatibility with CMOS fabrication technology and its potential to monolithically integrate electronics and photonics. However, silicon photonics does not address all the requirements of these emerging applications, mainly due to silicon's indirect bandgap, which prevents efficient light emission.

Even though the generation of mid-IR light sources is still challenging, several routes to overcome this have emerged in the past years, including the use of third order non-linearities to generate supercontinuum (SC) sources, the development of GeSn lasers emitting in the 2 – 3 μm wavelength range, and the hybrid integration of quantum cascade lasers (QCL) on Si. Despite this promising achievements, these approaches have some limitations. For instance, they either require an external high-power pulsed laser (for SC generation), exhibit a limited wavelength range (as in the case of GeSn lasers) or involve complex hybrid integration (as in the cases of GeSn and QCL).

Nevertheless, preliminary results have demonstrated strong emission of rare earth (RE)-dope chalcogenides glasses (ChG) under near-IR pumping (Bodiou et al. 2018) and the ease of integration of these materials onto Si waveguides (Serna et al. 2019). These results open a new pathway for the development of broadband and flexible mid-IR sources on Si platform by combining ChG wide mid-IR transparency, mid-IR emission from RE-ions and silicon photonics platform.

This work is part of the KASHMIR project, which aims to explore a novel approach for developing on-chip broadband mid-IR sources and tunable lasers by exploiting the hybrid integration of emitting rare earth (RE)-doped chalcogenides with sub-wavelength silicon photonics nanostructures. The project is a collaborative work between the Centre de Nanosciences et de Nanothecnologies (C2N), the Institute des Sciences Chimiques de Rennes (ISCR) and the Institute Foton.

In this context, the objectives of the master's thesis are:

- The theoretical study of sub-wavelength engineering waveguides and simulation work to extract the effective index and band structure.
- The design, fabrication, and characterization of metamaterial cladding waveguides.
- The theoretical study of supercontinuum generation (SCG) and its numerical simulation.

The realization of the master thesis was carried out at the Centre de Nanosciences et de Nanotechnologies (C2N) in Palaiseau, France.

1.2 Manuscript organization

Chapter 1 presents the motivation and the objectives of the final master's work. It also reviews the state-of the-art in several platforms used for mid-infrared photonic integration and mid-infrared light sources.

Chapter 2 introduces the working principle of sub-wavelength structures. Furthermore, it presents the computation of the effective refractive index and band-structure, through different simulation methods including FDM, varFDTD and 3D-FDTD.

Chapter 3 focus on the design, fabrication, and characterization of silicon waveguides with metamaterial cladding. Moreover, it provides a detailed description of the fabrication process and the characterization setup. Finally, it discusses the transmission results obtained from experimental characterization.

Chapter 4 reviews the principles of supercontinuum generation (SCG), group velocity dispersion (GVD), and self-phase modulation (SPM). It also covers dispersion calculations carried out thorough both bandstructure and effective refractive index simulations, along with SCG simulations based on FDM dispersion results.

Chapter 5 will present the conclusions of the master's thesis and provide perspectives for future studies.

1.3 State-of-the-art of mid-infrared photonics

1.3.1 Mid-infrared platforms

Silicon-on-insulator (SOI) is the preferred silicon photonics platform; however, its use in the mid-infrared is affected by the absorption of the silica cladding beyond 4 μm (J. Soler Penadés et al. 2018). Several alternatives offering a broader transparency range in the mid-IR have been proposed, such as silicon on sapphire (SOS), chalcogenides, silicon on silicon nitride (SOSN), germanium on silicon (GeSi), between others. Figure 1.1 presents the transparency windows of several materials in the mid-infrared range.

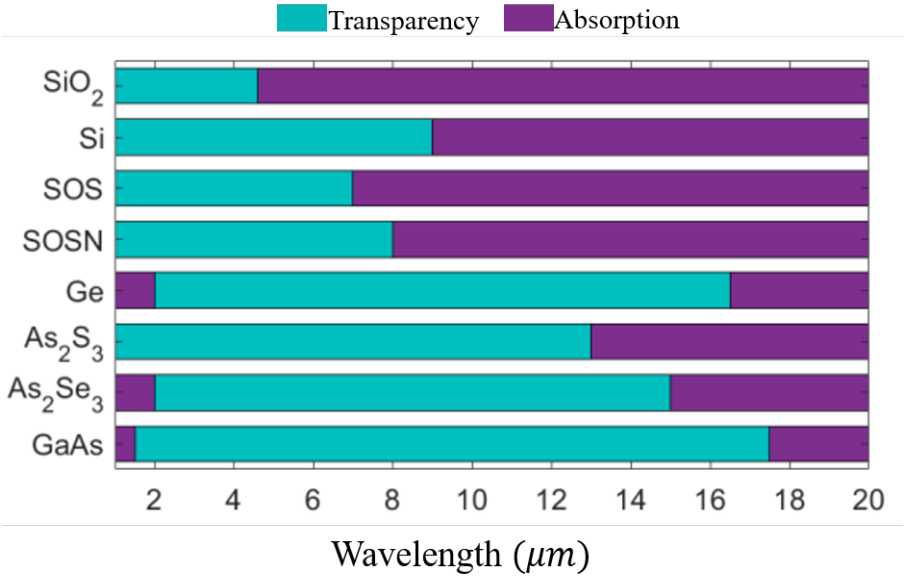

Figure 1.1 *Transparency window in the mid-IR range of multiple materials. The turquoise area stands for transparency, meanwhile the violet one represents high absorption (Thi-Thuy 2022).*

Silicon-on-insulator (SOI)

Silicon-on-insulator (SOI) is the preferred platform for optical telecommunications. It consists of a crystalline silicon layer on top of a buried oxide (BOX) layer made of silica (SiO_2). The large index contrast between Si (n_{Si} of 3.44 around 1550 nm wavelength) and SiO_2 (n_{Si0_2} of 1.44 around 1550 nm wavelength) provides a strong light confinement and allows a dense integration of photonic devices.

Even though silicon (Si) has a wide transparency range extending over 8 μm wavelength (Fig. 1.1), the use of silicon-on-insulator for mid-IR application is hampered by the silica absorption beyond 4 μm (J. Soler Penadés et al. 2018). Demonstrations of silicon-on-insulator (SOI) shown waveguides that can operate at 3.8 μm wavelength with propagation loss $\pm$ 0.2 dB/cm (Jordi Soler Penadés et al. 2015).

Miller et al. (2017) proposed a way to overcome this limitation by engineering the waveguide cross-section and the overlapping between the optical mode and the oxide under-cladding. By using a waveguide with cross-section 2300 nm $\times$ 4000 nm, they were able to achieve propagation loss below 1 dB/cm for wavelengths up to 6 μm, showing that the large core provides strong light confinement. The authors also shown the design of a microring resonator with an intrinsic Q $\approx 10^6$ at 3.8 μm wavelength with propagation losses below 1 dB/cm.

Suspended silicon

In order to exploit the full transparency window of Si spanning from 1.1 μm to 8 μm, suspended platforms can be employed. These platforms are fabricated by selectively removing the silica under-cladding of the SOI platform through hydrofluoric acid (HF) etching.

The implementation of suspended silicon for mid-IR offers multiple advantages. It benefits from the mature fabrications processes of SOI, the wide transparency range of silicon, strong non-linear effect, and negligible two-photon absorption beyond 2.2 μm wavelength. Additionally, it provides a high refractive index contrast between air ($n_{\text{air}} \approx 1$) and silicon ($n_{SiO_2} \approx 3.44$).

Figure 1.2 presents a schematic of the main approaches proposed for the fabrication of suspended silicon waveguides. Figure 1.2 (a), the rib waveguide, consists of a series of periodic holes etched on both sides of the waveguide core, allowing hydrofluoric acid (HF) penetration for. This structure, studied by Cheng et al. (2012), exhibited a propagation loss of 3 $\pm$ 0.7 dB/cm at a wavelength of 2.75 μm.

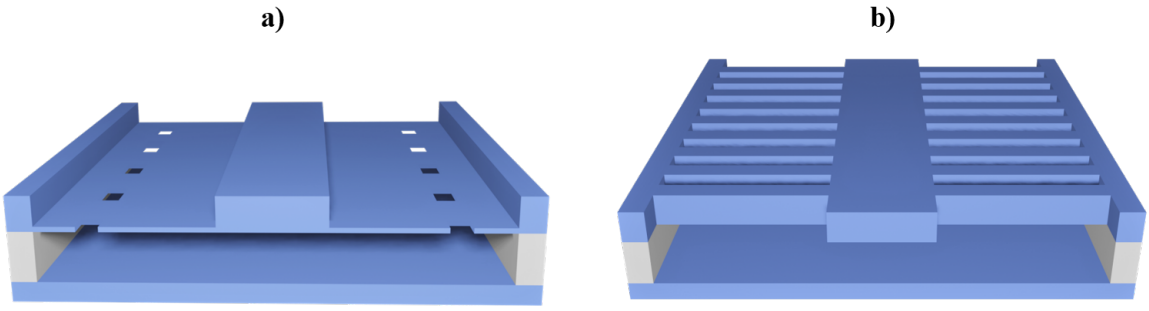

Figure 1.2 *Schematic of the suspended waveguides.(a) RIB waveguide, (b)Sub-wavelength grating (SWG) cladding waveguide.*

The second approach involves the implementations of sub-wavelength granting (SWG) structures as the cladding (see Figure 1.2 (*b*)). This SWG cladding serves three primary functions: I) lowering the effective index (n_{eff}) of the material, allowing light confinement, II) allowing for the penetration of HF for SiO_2 BOX removal, and III) providing mechanical stability after the removal of the silica layer.

Penades et al. (2016) implemented the suspended silicon SWG-cladded waveguide at 3.8 μm wavelength, achieving a low propagation loss of 0.82 dB/cm (Figure 1.3 b)). More recently, Thi-Thuy (2022) demonstrated a suspended structure with propagation losses of 1 – 2.5 dB/cm for a wavelength rage between 5 and 7 μm (Figure 1.3 c)).

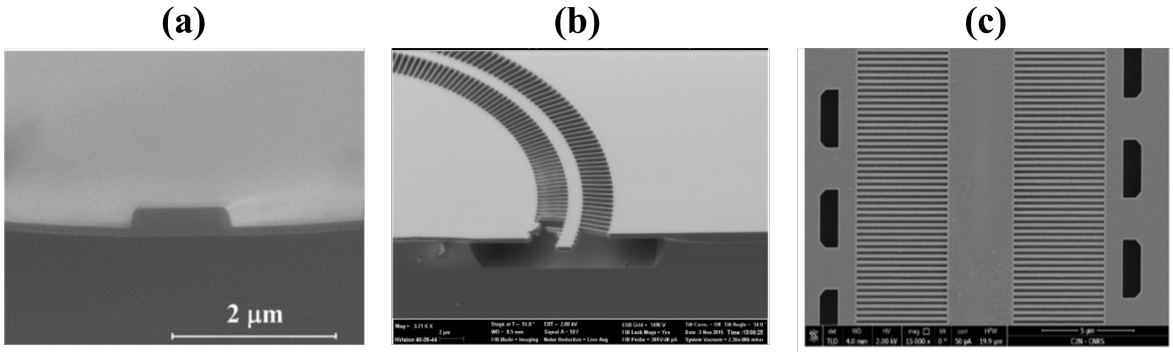

Figure 1.3 *Scanning electron microscope (SEM) images of: (a) suspended rib waveguide (Chang et al. 2012) ,(b) suspended SWG waveguide (Penades et al. 2016), and (c) suspended SWG waveguide (Thi-Thuy 2022).*

Chalcogenides

Chalcogenide glasses (ChGs) such as As_2S_3 and As_2Se_3 in Figure 1.1, are amorphous compounds which contain one or more chalcogen elements, such as sulphur, selenium, or tellurium, bonded with As, Ga, Sb, or Ge (Seddon 1995). They are known for their high infrared transparency, refractive index and optical nonlinearity,

making them attractive candidates for mid-IR applications. However, its application can be compromise due to their low thermal stability, low chemical durability and photosensitivity (Carlie et al. 2010).

Chalcogenide glasses can be integrated in a wide range of mid-IR transparent substrates such as calcium fluoride (CaF_2), sulphide glass (As_2S_3), lithium niobate ($LiNbO_3$), silicon, and sapphire (Gutierrez-Arroyo et al. 2016). Furthermore, through composition engineering it is possible to adjust their refractive indices, allowing them to serve as both waveguide core and cladding.

Ma et al. (2013) presented low loss GeAsSe rib waveguides achieving low propagation loss of 0.3 dB/cm at 5 μm wavelength. GeSbSe ridge waveguides, with single mode optical propagation at 7.7 μm and optical propagation losses 2.5 dB/cm, have been reported by Gutierrez-Arroyo et al. (2016).

Germanium

Germanium (Ge) is a group-IV semiconductor considered a strong candidate for the development of mid-infrared photonic devices due to its broad transparency range from $\approx$ 2 to 16 μm wavelength (see Figure 1.1). Ge- based platforms, including germanium on silicon (GeOS), germanium on insulator (GeOI) and germanium on silicon nitride (GeOSN), among others, have been extensively studied for mid-IR applications.

The GeOS platform is composed by a silicon cladding and a germanium core. Chang et al. (2012) demonstrated GeOS waveguides with losses in the range of 2.5-3.0 dB/cm at 5.8 μm wavelength for transverse magnetic (TM) polarization mode. Additionally, Mashanovich et al. (2017) achieved GeOS waveguides with a low propagation loss of 0.6 dB/cm at wavelength of 3.8 μm.

Germanium on insulator (GeOI) rib waveguide are demonstrated by Kang, Takenaka, and Takagi (2016) at 2 μm wavelength with 1.4 dB/cm propagation loss. Germanium on silicon nitride (GeOSN) has also been widely studied, e.g. W. Li et al. (2016). These platforms provide high index contrast, enabling strong light confinement. However, their use is constrained by the absorption of SOI and of silicon nitride at longer wavelengths.

1.3.2 Mid-infrared light sources

Integrating light sources in silicon has always been a great challenge in silicon photonics due to Si indirect bandgap. Over the past few years, several options to integrate mid-IR light sources on silicon have emerged, including:

i Quantum cascade lasers (QCLs)

ii Heteroepitaxy of semiconductors on Si such as GeSn lasers.

iii Nonlinear frequency generation e.g. frequency comb and supercontinuum generation sources.

iv The use of rare earth (RE) dope chalcogenide materials emitting in the mid-infrared.

This section contains a brief description of the light sources applied on MIR photonics.

Quantum cascade lasers

Quantum cascade lasers (QCLs) have undergone rapid development since their invention in the mid-1990s (Faist et al. 1994). QCLs are based on inter-sub-band (ISB) transitions in semiconductor heterostructures, enabling them to operate across a wide range of the electromagnetic spectrum, from mid-IR to THz. This is achieved though the engineering of the geometry and composition of the quantum wells.

Mid-infrared quantum cascade lasers are mostly based on indium-based heterostructures (InGaAs/InAlAs), capable of emitting light up to 11 μm. This technology provides discrete and tunable lasers, forming the basis of mid-IR photonics (Yao, Hoffman, and Gmachl 2012).

QCL have been successfully integrated on silicon based platforms. For example, in Spott et al. (2017), a Fabry-Perot QCL bonded to Si on silicon nitride operating around 4.8 μm is shown to emit up to 31 mW in pulsed mode at 60 °C.

More recently, Coutard et al. (2020) reports distributed feedback quantum cascade lasers (DFB-QCL) source arrays emitting around 7.4 μm with threshold current density below 3 kA.cm^{-2} and output power of 1 mW fabricated on 200 nm Si wafers following standard CMOS manufacturing processes.

Heteroepitaxy of semiconductors on Si: GeSn lasers

Heteroepitaxy of non Si-semiconductors on silicon enables the monolithic integration of photonic devices onto the silicon platform, leveraging the optoelectronic properties of the non Si-materials.

Ge combining advantages in terms of nonlinear index (an order of magnitude larger than Si) and a broader transparency window. GeSn/SiGeSn heterostructures are considered promising candidates for implementing monolithic lasers on Si and enabling full photonic integration since it has been shown that when the concentration of Sn exceeds 8 %, GeSn turns into a direct bandgap material able to display light emission. Sn content and strain can also help to elevate the lasing temperature, as reported in Chrétien (2019). More recently, Bjelajac et al. (2022) have

shown that lasing at room temperature up to 300 °K can be obtained with a GeSn alloy containing 17 % Sn. By carefully engineering carrier and optical confinement in p-i-n GeSn/SiGeSn heterostructures, Zhou et al. (2020) demonstrate electrically injected lasing at peak wavelength of 2.3 μm with an external quantum efficiency (EQE) estimated to 0.3 % at 10 °C.

Nonlinear mid-IR sources

Many nonlinear effects have been employed to generate mid-IR light sources including four wave mixing, frequency combs (M. Yu et al. 2016), stimulated Raman scattering (Raghunathan et al. 2007) and supercontinuum generation (Kou et al. 2018).

Frequency combs generation is a coherent light source that emits a broad spectrum of discrete, evenly spaced narrow lines. These sources originally developed in near-IR are now extended to the mid-IR, as shown in N. Li et al. (2018). Frequency comb sources have been implemented using a variety of physical phenomena such as nonlinear frequency conversion, phase-locked states in QCL, mid-IR mode locked lasers, between others.

Supercontinuum generation (SCG) is another method that continues to be extensively studied as a mean to provide broadband and coherent light. Due to the large nonlinear index of silicon ($n_2 = 6.3 \times 10^{-18}$ m^2 W^{-1}) and high mode confinement resulting from silicon's high refractive index (n $\approx$ 3.44 at 1.55 μm wavelength), SCG has been reported to achieved a bandwidth of 1.1 – 2.8 μm on standard silicon-on-insulator platform (Wei et al. 2020).

Nevertheless, the use of SOI can limit the spectral broadening due to SiO_2 absorption; several schemes have been proposed to overcome this, such as the incorporation of sapphire as lower cladding material, the use of Ge and SiGe, and the implementation of suspended silicon waveguides. A more extensive explanation of the supercontinuum generation (SCG) phenomena and light sources based on it is presented in 4.

Rare-earth doped chalcogenides

Another alternative to integrate mid-IR sources into silicon photonics (SiP) relies on the use of rare-earth (RE)- doped chalcogenides as the gain medium. These include erbium, dysprosium, praseodymium, terbium, and samarium, which are considered the most prominent ions for mid and long infrared emission under near-infrared excitation. Demonstration (Hendriks et al. 2021) of lasing and net optical gain have been achieved at various near-IR wavelengths ranging from 1.1 to 2.1 μm by using RE doped aluminium oxide (RE^{3+}:Al_2O_3).

However, amorphous Al_2O_3 transmission is limited to wavelengths below ≈ 5 μm and presents high phonon energy. Furthermore, Al_2O_3 deposition on Si is often performed on a heated substrate with temperatures up to 800 °C (Worhoff et al. 2009) which can damage the Si photonic structures.

In order to overcome these limitations and extend the emission range further in the mid-IR, Bodiou et al. (2018) proposed praseodymium-doped selenide thin films deposited on thermally oxidized silicon wafers, which record broadband guided mid-infrared photoluminescence above 4 μm under optical pumping at 1.55 μm wavelength.

More recently, Louvet et al. (2020) reported mid-IR photoluminescence between 2.4 and 4.5 μm for waveguides based on Ga-Ge-Sb-Se amorphous thin films doped with praseodymium ions (Pr^{3+}) using near-IR light at 1.5 μm as the pump beam.

The ease of integrating chalcogenide glasses onto silicon substrates has also been shown, as presented in Serna et al. (2019), where they show the homogeneous infiltration of As_2S_3 chalcogenide glass into silicon slot waveguides. Thus, chalcogenide materials, in addition to their broader transmission window, offer the advantage of being deposited at room temperature providing compatibility with back-end of line (BEOL) CMOS process (T $\leq$ 500 °C) which could enable scalable integration and potential for low-cost high volume mass production.

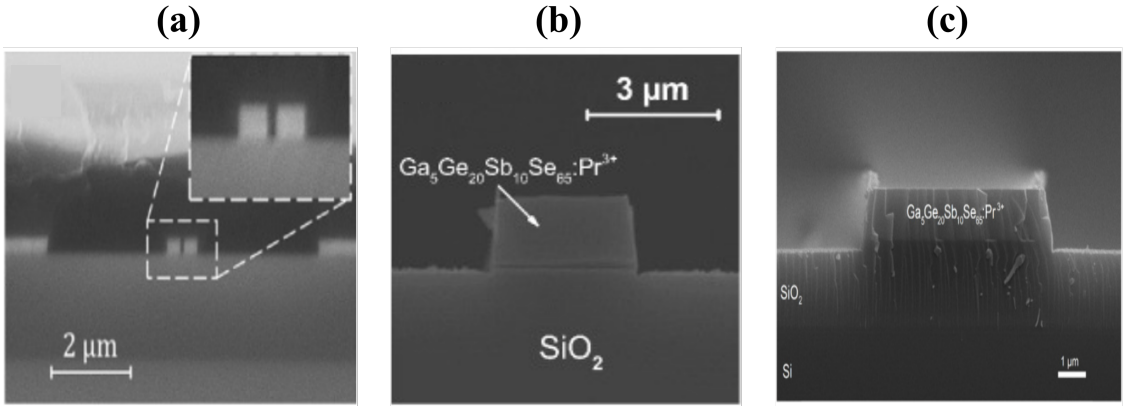

Figure 1.4 *Scanning electron microscope (SEM) images of: (a) Si strip waveguide covered in annealed As_2S_3 glass (Serna et al. 2019), (b) Pr^{3+}-doped $Ga_5Ge_{20}Sb_{10}Se_{65}$ ridge waveguides on SiO_2 (Bodiou et al. 2018), and (c) cross-section of $Ga_5Ge_{20}Sb_{10}Se_{65}$:$Pr^{3+}$ ride waveguide on SiO_2/Si substrate (Louvet et al. 2020*

2 Mid-infrared SWG-cladded silicon waveguides

Subwavelenght optics has been proposed for more than half a century (Rytov 1956). Since its first demonstration in silicon photonics (P. Cheben et al. 2006), it has been continuously applied to overcome devices limitations, benefiting from the rapid development of fabrication technologies.

This chapter will introduce the working principle of the subwavelenght regime, discuss the design of suspended waveguides with metamaterial cladding and explain the simulation techniques used in their study. Finally, the chapter will present the simulation results of effective refractive index (n_{eff}) and bandstructure.

2.1 Introduction

Sub-wavelength gratings (SWG) metamaterials have gained great interest due to their capability to tailor material properties such as refractive index, dispersion, and anisotropy by engineering geometrical parameters like the grating teeth length or the period. The length of the grating period and the wavelength determine whether the structure will diffract light or behave as a homogeneous medium.

The combination of sub-wavelength engineering and advanced lithography fabrication has made it possible to demonstrate several SWG-based optical devices, including multimode interference couplers (Maese-Novo et al. 2013), grating couplers, mode converters, etc (Halir, P. Bock, et al. 2014).

Figure 2.1 presents scanning electron microscope (SEM) images of various SWG based photonic devices. Figure 2.1 (a) shows the first reported subwavelenght grating silicon waveguide (P. J. Bock et al. 2010). The structure, demonstrated in 2010, has a period of 300 nm and a duty cycle DC = 0.33, and a propagation loss of 3 dB at 1.5 μm wavelength. Figure 2.1 (c) presents an image of the first SWG-based suspended waveguide with a grating period of 300 nm and propagation loss of 3.4 dB/cm at a wavelength of 3.8 μm.

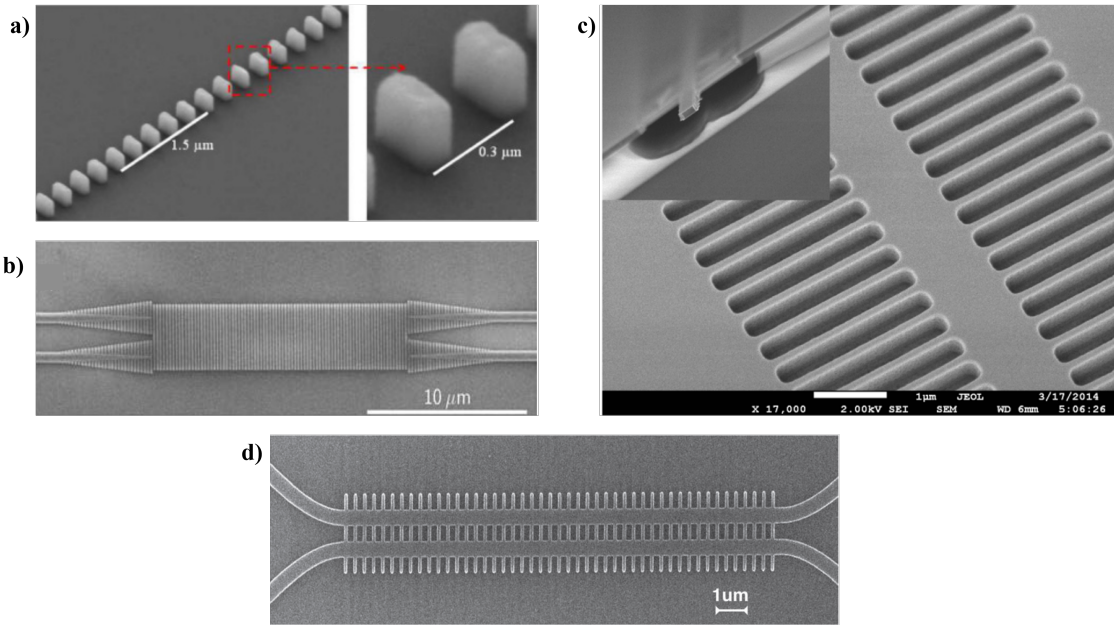

Figure 2.1 *a) SEM image of SWG straight waveguide on SOI with Λ of 300 nm (P. J. Bock et al. 2010),* ***b)*** *SEM image of a SWG multimode interference coupler (Halir, Pavel Cheben, et al. 2016),****b)*** *SEM image of the first SWG-cladded suspended silicon waveguide(J. Soler Penades et al. 2014), and* ***d)*** *SEM image of a SWG directional coupler (Wang et al. 2016).*

2.1.1 Sub-wavelength gratings (SWG) working principle

Let us consider the case of the periodic structure presented in Figure 2.2, consisting of alternating slabs of dielectric material with refractive index n_1, where a is the slab width and Λ the grating period.

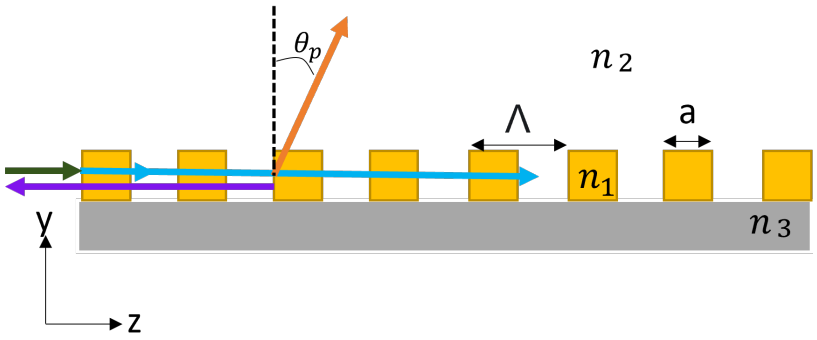

Figure 2.2 *2D representation of a periodic structure with grating period Λ, dielectric slab length a and duty cycle (DC) = $\frac{a}{\Lambda}$. Defining input (green), reflected (purple), radiated (orange) and transmitted (blue) light beams.*

Depending on the length of the grating period Λ compared to the wavelength λ, this structure can: *a)* radiate, *b)* reflect or *c)* transmit the light, acting as a homogeneous anisotropic media (Halir, P. Bock, et al. 2014).

a) In radiation regime, the period is longer than half the wavelength $\Lambda > \lambda/2$ and the light is scattered away from the structure.

b) In the Bragg reflection regime, the grating period is equal to half the wavelength $\Lambda = \lambda/2$ and light is back-reflected in the counter propagation direction.

c) In the subwavelenght regime, the period is smaller than half the wavelength $\Lambda < \lambda/2$,the reflection, and diffraction effects are suppressed and light propagates through the structure.

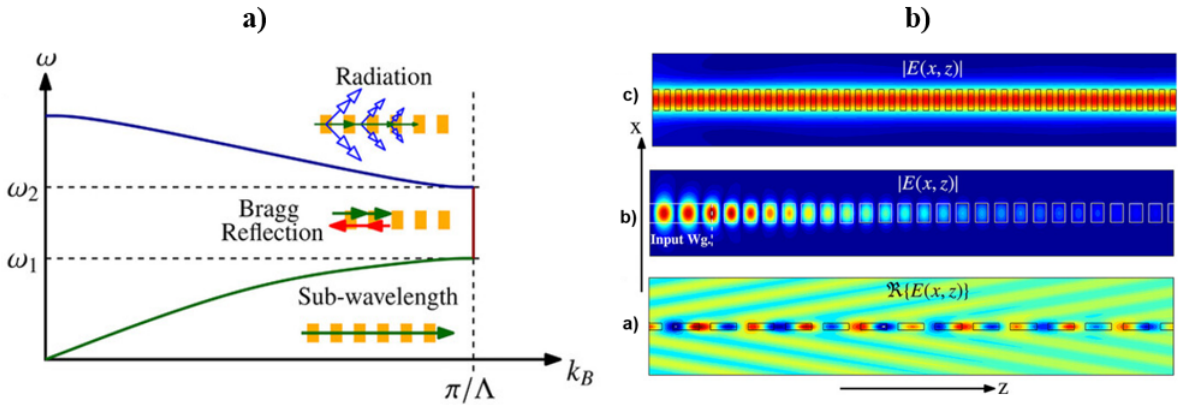

Figure 2.3 *Schematic of a) the first Brillouin zone dispersion diagram of light propagating lengthwise through a structure with period* Λ *and b)electric field profiles for the three different regimes: radiation, reflection and subwavelenght (Halir, P. Bock, et al. 2014).*

Propagation of light along SWG structures can be described using the Floquet-Bloch formalism (Gonzales 2020) since it is similar to the propagation of an electron through a periodic crystal. Let's consider light propagation in z direction, the Floquet-Bloch mode is then written as:

$$\vec{E}(x, z + \Lambda) = \vec{E_B}(x, z)exp(-\gamma_B \Lambda) \tag{2.1}$$

where $\gamma_B = \alpha_B + j\kappa_B$ is the complex propagation constant, where α_B and $\kappa_B = (2\pi/\lambda) * n_B$ are the attenuation and propagation constants respectively. The effective index n_B of the Floquet-Bloch mode can be obtained through simulations based on finite-difference time domain (FDTD) method.

Figure 2.3 *(a)* presents the dispersion diagram in the first Brillouin Zone (BZ) of a periodic waveguide. At high frequencies, $\omega > \omega_2$ the mode becomes leaky and is radiated out of the structure. The band-gap $\omega_1 < \omega < \omega_2$ corresponds to the Bragg regime, where light can not propagate through the structure and is reflected backwards. Finally, at low frequencies $\omega < \omega_1$ the propagation constant (k_B grows) monotonically meaning that the periodic waveguide behaves as a conventional one and light propagates through the structure, it operates in sub-wavelength regime.

Light incident on the grating can have electric field polarization parallel or perpendicular to the periodic structure, their equivalent refractive indices are given by Rytov's equations (Rytov 1956) :

$$n_{\parallel}^2 = \frac{a}{\Lambda} n_1^2 + (1 - \frac{a}{\Lambda}) n_2^2, \tag{2.2}$$

$$\frac{1}{n_{\perp}^2} = \frac{a}{\Lambda}\frac{1}{n_1^2} + (1 - \frac{a}{\Lambda})\frac{1}{n_2^2}, \tag{2.3}$$

where a is the width of the slab of the material with refractive index n_1 and Λ the period.

2.2 SWG-cladded waveguides design

This section presents the geometry definition of the suspended silicon waveguides with metamaterial cladding, as well as the simulation strategies used for their study.

2.2.1 Geometry definition

The main motivation for implementing SWG-cladded waveguides is to have control over the properties of the cladding, which can be done by engineering its geometry. These structures can be fabricated in a single etch step, but they require the precise definition of small size holes over relatively thick silicon layers.

The SWG-cladded waveguide parameters, presented in Figure 2.4, are the core width (W_{core}), the cladding width (W_{clad}), the buried oxide thickness layer (t_{BOX}), the silicon thickness layer (t), the length of the gratin teeth (a), and the length of the grating period (Λ). The gap length between a grating tooth and another is denoted l_g and is given by the difference between the period (Λ) and a, $l_g = \Lambda - a$.

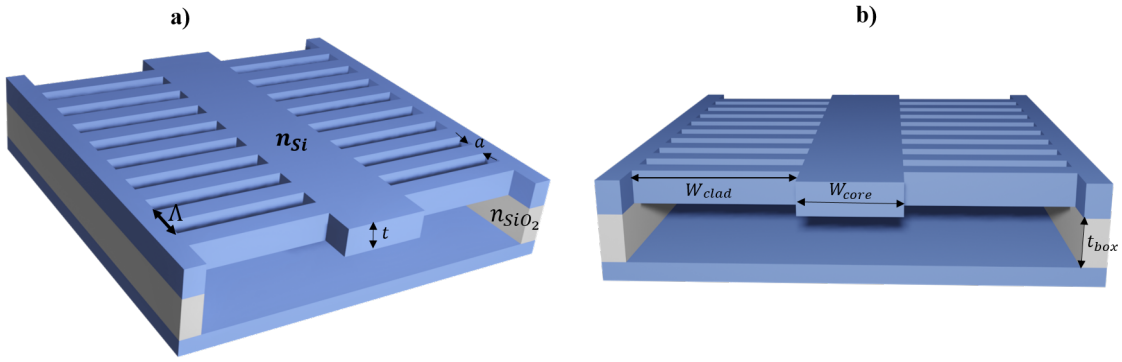

Figure 2.4 *Schematics of a suspended SWG-cladded waveguide. Where Λ is the period, t the silicon thickness, W_{clad} the cladding width, W_{core} the core width and n_{Si} the refractive index of silicon.*

Silicon-on-insulator wafers with different silicon (Si) thickness (200 nm, 300 nm, 500 nm, 700 nm and 1500 nm) are available in C2N cleanroom. A larger Si thickness allows a better confinement for long wavelengths, however it also involves higher difficulty in etching the subwavelenght size structures. A SOI wafer with silicon thickness of 700 nm and buried oxide box (t_{BOX}) of 3 μm was selected as a good compromise solution.

In order to ensure mechanical stability, the width of the cladding W_{clad}, is fixed at 5 μm. We will consider multiple values of the core width, W_{core}, along with different duty cycles, DC = a/Λ to assess the system's performance.

2.2.2 Band structure and effective refractive index simulations

Different simulation strategies were applied for the study of the SWG cladded suspended waveguides. First, we utilized a simplified model based on the equivalent refractive index method, followed by simulations with a variational finite difference time domain (varFDTD) solver and full-vectorial three-dimensional simulations using finite difference time domain (3D-FDTD).

Finite difference method (FDM) for effective index and 2D modal analysis.

Finite Difference Method (FDM) allows computing the field profiles, effective index and loss of a waveguide by solving Maxwell's equations over a cross-sectional mesh of the system (Optics 2023c). The effective index method provides an insight of how the optical mode is affected by the geometrical parameters of the waveguide, like the SWG period or the core width.

The periodic structure can be modelled as a homogeneous non-periodic structure by defining an equivalent strip waveguide with the same cross-section as the SWG-cladding but with an equivalent refractive index (n_{clad}). We considered light with electric field polarization parallel to the periodic interface, therefore the index n_{clad} can be computed through Rytov's equation (Rytov 1956):

$$n_{clad}^2 = \frac{a}{\Lambda} n_{Si}^2 + (1 - \frac{a}{\Lambda}) n_{air}^2, \tag{2.4}$$

where n_{Si} and n_{air} are the refractive indexes of silicon and air, a is the length of the granting teeth and Λ is the period.

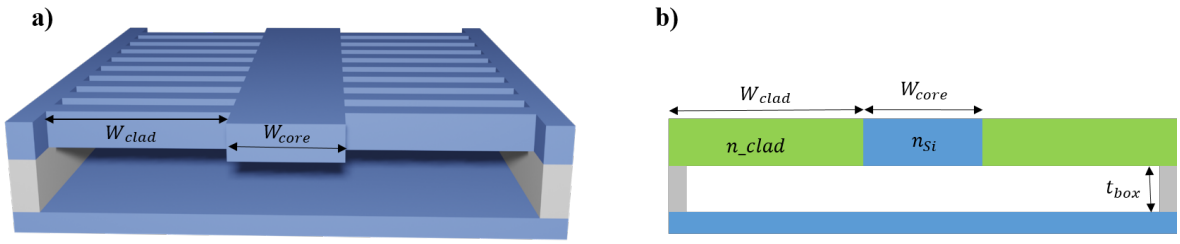

Figure 2.5 *a)Illustration of a SWG-suspended waveguide and* ***b)****cross-section of the waveguide with equivalent refractive index* n_{clad} *given by Eq. 2.4.*

For the simulation, we considered a mesh of Δ x $\times$ Δ y $\times$ Δ z = 10 nm $\times$ 10 nm $\times$ 10 nm and a background refractive index of 1. The frequency analysis for the selected mode (TE_{00}, TE_{10}, TM_{00} and TM_{10}) were performed in a frequency range from 3 to 8 μm. FDM computes the modal effective refractive index through

$$n_{\mathbf{eff}} = \frac{c}{v} = \frac{\beta}{k_0}. \tag{2.5}$$

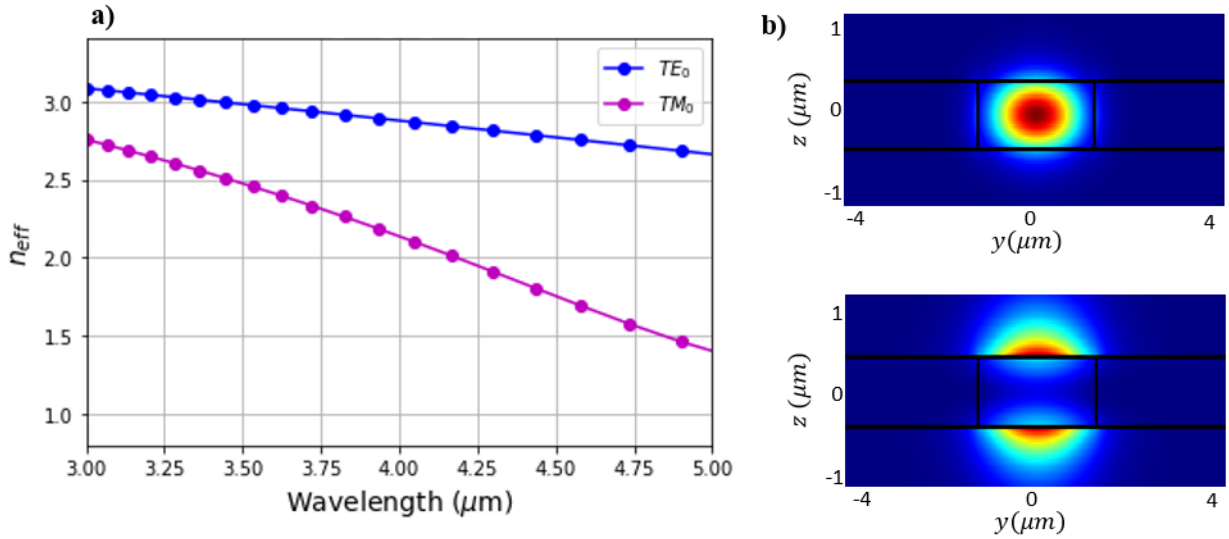

Figure 2.6 ***a)****FDM results of the effective refractive index with respect to the wavelength for the fundamental TE and TM modes.* ***b*** *Field profiles ($|E^2|$) of* TE_{00} *(top) and* TM_{00} *(bottom) at a wavelength of 5 μm.*

Figure 2.6 (a) presents the effective refractive index of the fundamental transverse-electric (TE) and transverse-magnetic (TM) polarized modes computed with FDM using the same n_{clad} for both polarizations, with a core width of W_{core} = 2.5 μm and a cladding width W_{clad} = 5 μm. In this case, a duty cycle (DC = a/Λ) of 0.5 is considered, with a period Λ of 300 nm and a length of the gratin teeth a of 150 nm. Figure 2.6 (b) shows the fields profiles for TE and TM modes at a wavelength of 5 μm.

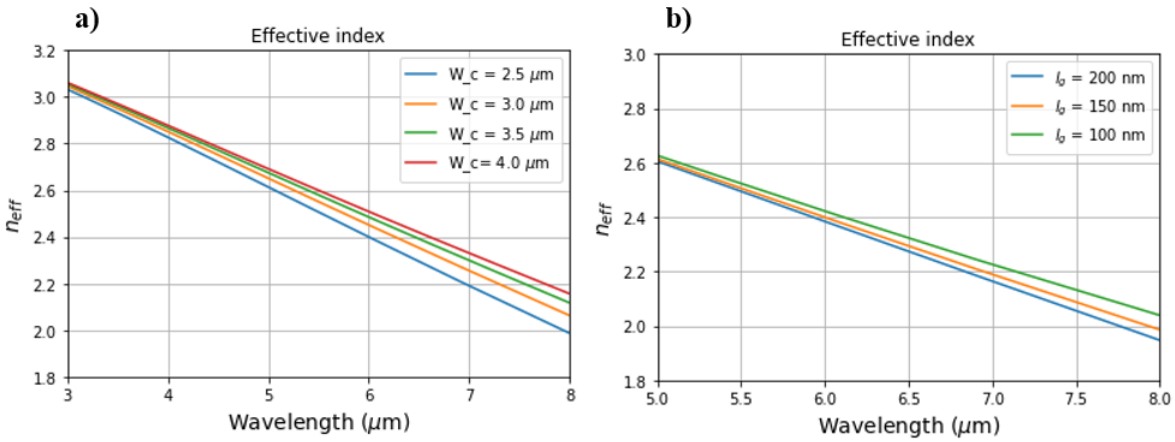

Figure 2.7 *Comparison of the effective refractive indices for:* ***a)*** *Multiple core widths with period* Λ *=300 nm, and* ***b)*** *Multiple periods and core width* W_{core} *= 2.5* μ*m, computed through 2D modal analysis.*

Figure 2.8 shows the computed effective index (n_{eff}) of the fundamental TE_{00} and TM_{00} modes and the first higher order modes TE_{10} and TM_{10} as a function of wavelength for different core widths and duty cycle of 0.5.

In Figure 2.7 (a), we compare the effective refractive index (n_{eff}) of the periodic structure with duty cycle of 0.5 for different core widths. Figure 2.7 (b) presents the change of n_{eff} for a system with W_{core} of 2.5 μm and varied duty cycles.

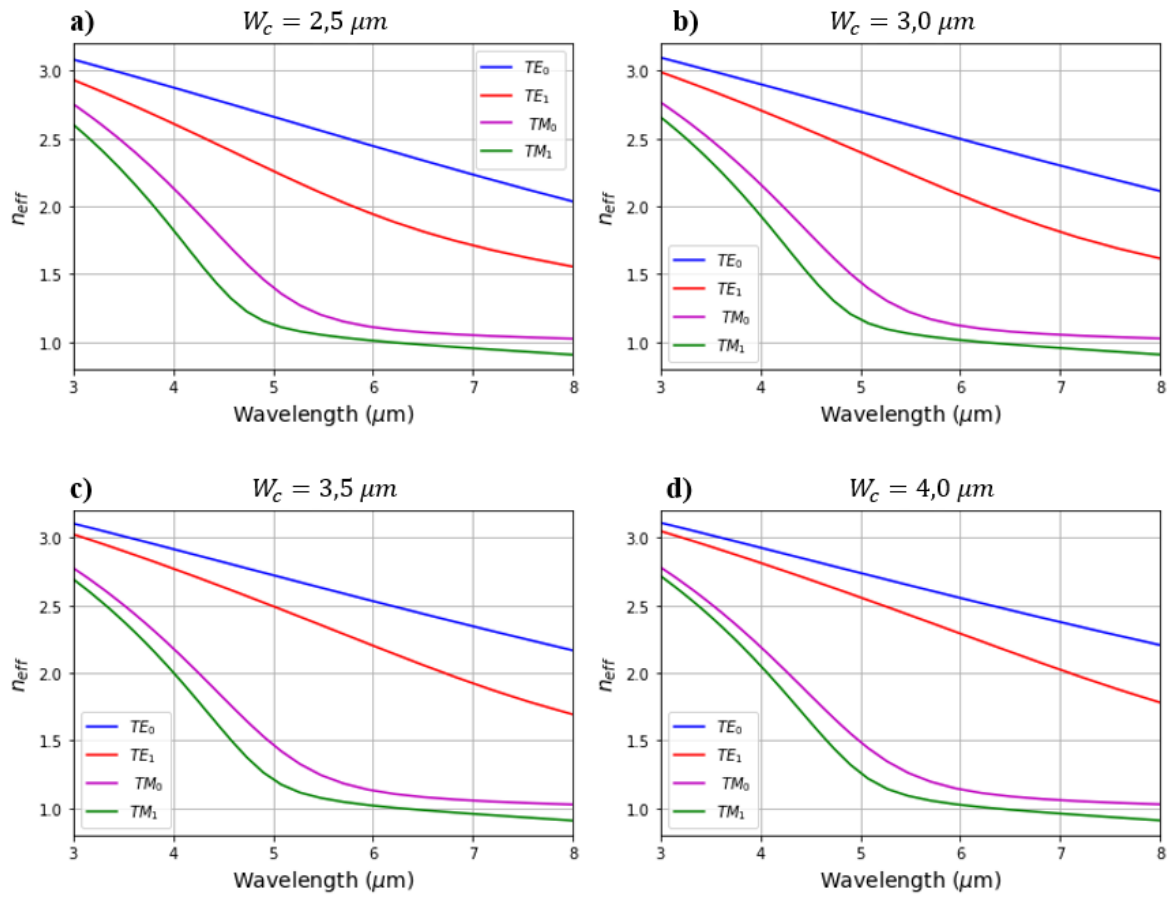

Figure 2.8 *Effective indices of the fundamental and first TE and TM polarization modes as functions of the wavelength for a system with period* Λ*= 300 nm and duty cycle DC (a/*Λ*) of 0.5. The core widths (*W_{core}*) considered are: (a) 2.5 µm, (b) 3.5 µm, (c) 3.0 µm, and (d) 4.0 µm.*

2.5 varFDTD and full vectorial 3D-FDTD simulations

The effective index method allowed us to run several simulations in a short period of time using a simplified model. To implement more accurate simulations, we used variational finite-difference time-domain (varFDTD) solver (Optics 2023b), as well as full vectorial FDTD solver (Optics 2023a).

Variational finite-difference time-domain (varFDTD) collapses the 3D model into a 2D one with the help of a supplemental effective index (Optics 2023b), providing the precision of a 3D simulation with the speed of a 2D simulation. VarFDTD was used for preliminary studies of the system and to identify the correct symmetry for exciting only TE modes.

The full vectorial 3D-FDTD method is used to solve Maxwell's equations in the time domain. It does not make any approximations or assumptions about the system, resulting in high accuracy and versatility. We conducted precise bandstructure simulations using this method.

In section 2.1.1, it was mentioned that light propagation along SWG structures can be described through the Floquet-Bloch formalism, since the system can be considered as a 1D photonic crystal. The modes of the periodic structure can be described as $\vec{E} = \vec{E_\kappa}(x, y, z + \Lambda)exp(-i\kappa z)$, where κ is the Bloch wavenumber and Λ the grating period.

Both varFDTD and 3D-FDTD allow the study of the properties of an infinitely long waveguide by considering only one period (one unit cell). The bandstructure is determined by the propagation equation, which, for each wavenumber κ gives a set of frequency solutions. The first mode occupies the lowest allowed energy (frequency), with each subsequent mode increasing in energy. The band diagram represents the possible combinations of frequencies and wave vectors that can propagate (interact) with the periodic structure.

In order to excite all possible modes of the system, a dipole cloud source with randomly distributed orientations was used (see Figure 2.9). It is possible to study only modes with TE or TM polarization by choosing the dipole cloud type (electric or magnetic) and the appropriate symmetry conditions (Optics 2023d).

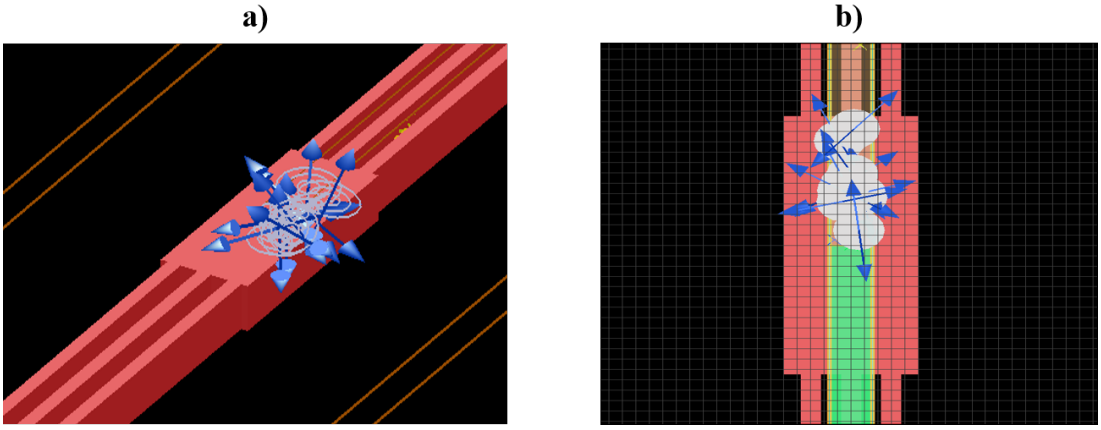

Figure 2.9 *Screenshots of the 3D simulation realized with Lumerical FDTD solver over one period: (a) Shows the perspective view, and (b) Shows the electric dipole cloud and antisymmetric symmetry.*

At frequencies where a mode (band) exist, the field will propagate indefinitely. At all other frequencies, the fields will disappear due to destructive interference. The bands are identified by applying the bandstructure analysis group, which contains randomly-distributed time field monitors. Each monitor records the field E(t) over time and conducts a Fourier transform analysis to determine the resonant frequencies. Subsequently, the bandstructure combines the Fourier transform time signals from each field component of each time monitor. Summing over several monitors ensures that all resonant frequencies are found, even if one of the monitors is located in a node of a particular mode. The field monitors exclude the effects of the source at the beginning and end of simulation (apodization).

During the bandstructure simulations, we utilized an electric dipole cloud source with a frequency range spanning from 20 to 100 THz. The simulation employed a mesh resolution of Δ x $\times$ Δ y $\times$ Δ z = 10 nm $\times$ 10 nm $\times$ 10 nm on the grating teeth within the simulation region. Periodic Bloch boundary conditions were applied in the direction of propagation, while perfectly matched layer (PML) conditions were implemented in the other directions. The background refractive index where not structure is specified is set to 1, representing air.

One simulation provides the spectrum for a single Bloch vector.To compute the bandstructure, we created a swept to ran simulations over a range of normalized k_x vectors from 0 to 0.2, where, $k_x = k^*\Lambda/2\pi$, Λ is the period and k the Bloch vector.

The effective refractive index (n_{eff}) can be computed from the bandstructure through,

$$n_{\text{eff}} = \frac{c}{\omega} k(\omega), \tag{2.6}$$

where c is the speed of light, ω the angular frequency and $k(\omega)$ the Bloch wavenumber.

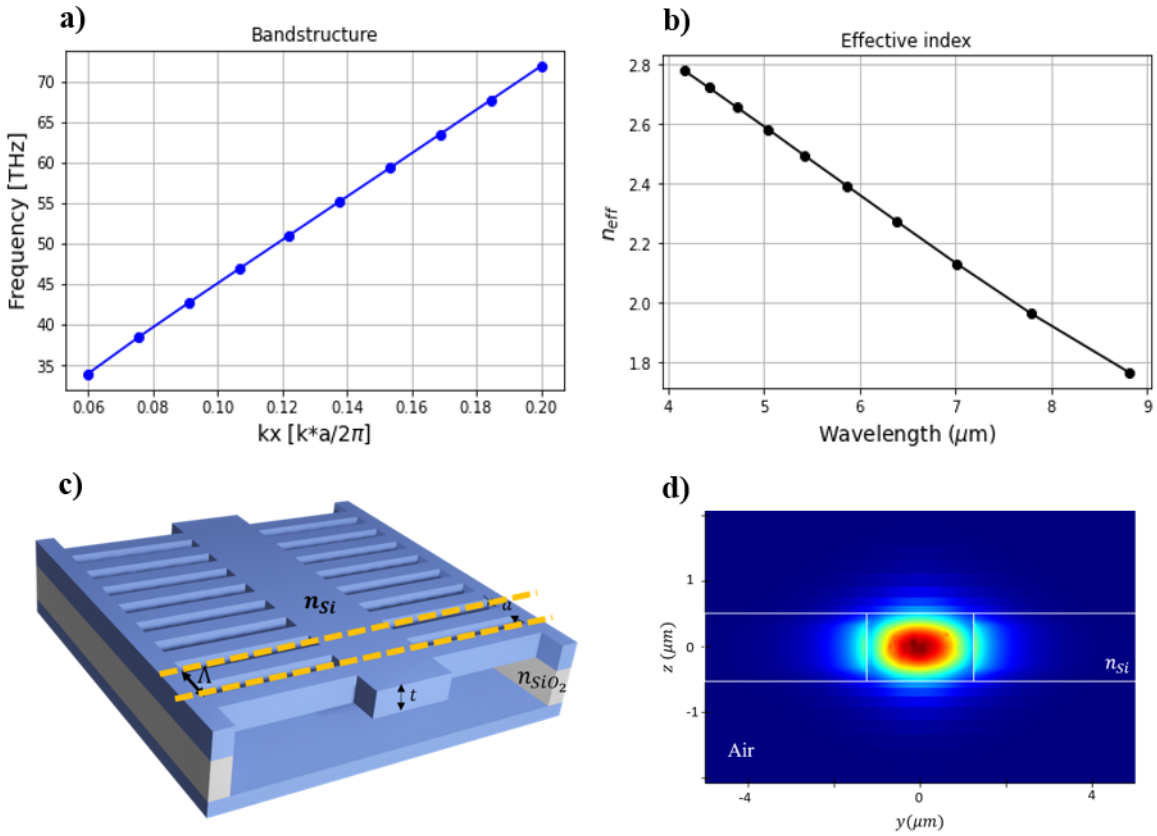

Figure 2.10 a) *Calculated bandstructure using 3D-FDTD of the suspended SWG-cladded waveguide with geometrical parameters: Λ = 300 nm, W_{clad} = 5 μm, W_{core} = 2.5 μm, DC = 0.5 and silicon thickness t = 700 nm.* ***b)*** *Calculated effective index as function of the wavelength using Eq. 2.6.* ***c)****Schematic view of the suspended waveguide* ***d)*** *Field profile of the fundamental TE mode over one period with a central wavelength of 4.7 μm.*

In Figure 2.10 we show the bandstructure and effective index computed using 3D-FDTD for the fundamental TE mode of a suspended SWG-cladded waveguide with the following geometrical parameters: core width W_{core} = 2.5 μm, cladding width W_{clad} = 5 μm, duty cycle of 0.5 with period Λ = 300 nm, and silicon thickness t_{Si} = 700 nm.

Figure 2.11 (a) shows the comparison of the effective refractive index (n_{eff}) of the periodic structure with a duty cycle of 0.5 for different core widths in a wavelength range from 5 to 8 μm. We can observe that increasing the core width also increases the effective refractive index.

In Figure 2.11 (b) we present the change in n_{eff} for a system with W_{core} of 2.5 μm and varying duty cycles. At wavelengths around 5 μm the difference in refractive index is not that noticeable, but it becomes more prominent at 8 μm wavelength. The system with a gap length of 100 nm (DC = 0.6) exhibits a higher effective refractive index, with a value of 1.8.

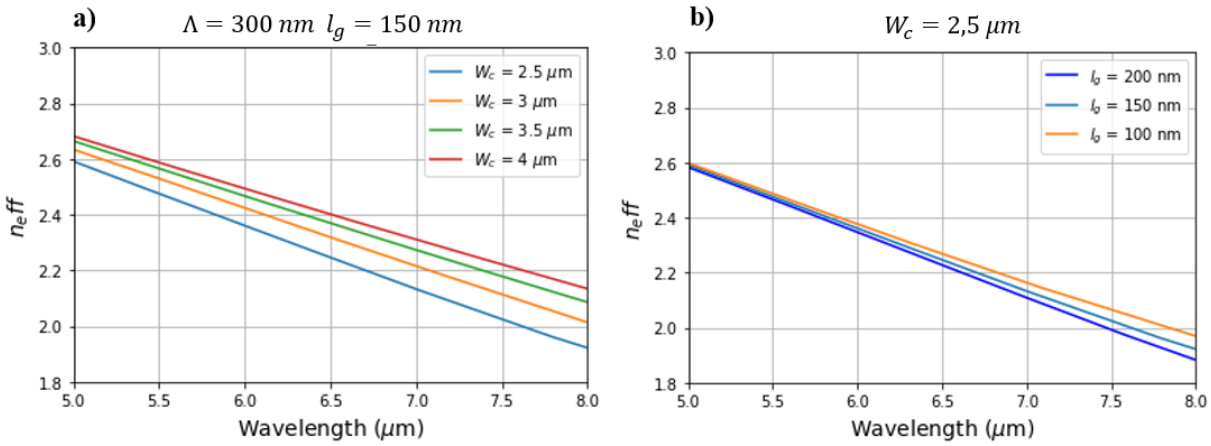

Figure 2.11 *Comparison of the effective refractive indices for:* ***a)*** *Multiple core widths with period* Λ = *300 nm, and* ***b)*** *Multiple periods and core width* (W_{core}) *of 2.5 μm, computed using 3D-FDTD.*

The results of the effective refractive index obtained through 3D-FDTD simulations agree with those computed using the finite difference method (FDM) solver. Full vectorial 3D-FDTD allow us to study the subwavelength structure with a better precision, however it is time and memory consuming and is not recommended for large parameter sweeps.

2.3 Summary

In this chapter, we introduced the working principle of the sub-wavelength regime and its application in silicon photonic devices. We defined the geometry of the SWG-cladded suspended waveguide and presented the numerical simulations techniques

used for its analysis.

We conducted several simulations in FDM and 3D-FDTD to analyse how the changes in geometrical parameters, such as the core width W_{core} and the duty cycle (DC=a/Λ), affect the bandstructure and effective refractive index. These parameters can be optimized for a given application, and a higher index contrast offers a higher mode confinement, enabling denser integration.

3 Sample fabrication and characterization

This chapter centres on the sample design, fabrication process, and optical characterization of SWG-cladded waveguides. It provides a detailed description of the fabrication steps and presents the mid-IR setup used during the characterization, as well as the transmission measurements.

3.1 Sample design

Based on the simulation results presented in Chapter 2 tapered SWG-cladded waveguides were designed using the Python GDS library. Waveguides with core widths W_{core} of 2.5, 3.0, 3.5, and 4.0 μm and period Λ = 250, 300, and 350 nm were designed for a sample with dimensions of 0.5 cm x 1 cm.

Tapers are fundamental components for realizing coupling between devices of varying dimensions, such as connecting two waveguides with different core widths or coupling light from the source to a device. Their primary function is to change the size and shape of the optical mode in order to achieve high couple efficiency. To accomplish this, the taper needs to operate adiabatically, allowing the waveguide mode to propagate through the taper without converting to high-order modes or radiation modes. This is achieved by gradually decreasing or increasing the size of the taper cross-section. For these reasons, we considered a taper with width W_{taper} of 20 μm and length L_{taper} of 500 μm.

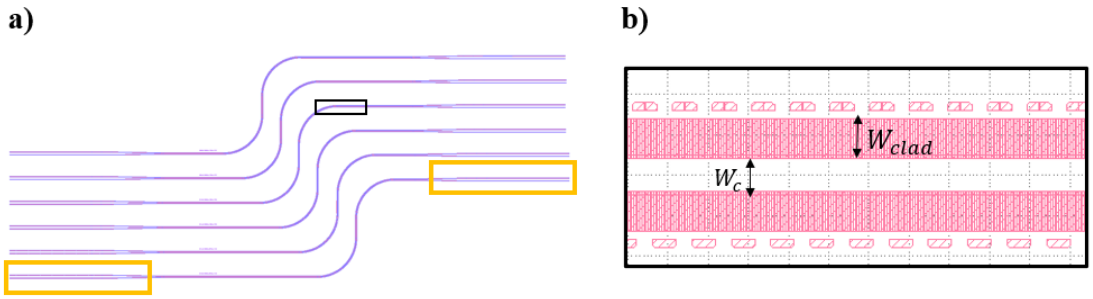

Figure 3.1 *GDS extract of* ***a)*** *waveguides structures, with orange rectangles marking the tapers and* ***b)*** *close up, core width (W_c), cladding width (W_{clad}) and liberation holes.*

Figure 2.10 (a) shows a section of the structures on the GDS file, with orange rectangles marking the tapers. In Figure 2.10 (b) the masks of the liberations holes for hydrofluoric acid penetration and the sub-wavelength structures can be appreciated.

The designed SWG-cladded waveguides have an "S" shape with approximately 90 degrees bends. To ensure adiabatic behaviour and avoid losses due to radiation,

the radius of curvature is chosen to be sufficiently large. The relation between the radius of curvature (R) and the angular discretization of the SWG structures ($\Delta\phi$) is: $R \approx \Lambda/\Delta\phi(\text{rad})$ (Penades et al. 2016).

3.2 Fabrication

The fabrication of the waveguides on SOI required multiple steps; a schematic of the process is presented in Figure 3

- **Cleaning**: The silicon-on-insulator (SOI) wafer is initially cleaned with acetone and isopropyl alcohol (IPA) to remove any contamination and ensure strong adhesion between the silicon layer and the photoresist. (Fig.3 a))
- **Spin coating**: The wafer is carefully placed inside the spin coating machine, and a few drops of photoresist are applied to it. Two types of photoresist can be used: positive or negative. The thickness of the photoresist layer can be controlled by the rotation rate of the spin coater. After spin coating, the wafer is put on a hotplate for baking. During this step, the photoresist is dried and strengthened.
- **Electron-beam Lithography**: Once the photoresist is applied, the wafer is cleaved to obtain a sample with the desired dimensions. An electronic lithography machine is used to transfer the GDS design onto the silicon layer. (Fig.3 c))
- **Developing**: In order to recover the pattern after the E-beam lithographic process, the sample is soaked into developing solution and then dried with N_2. (Fig.3 d))
- **Etching**: The sample is then transferred to the dry etching machine, where a thin layer of thermal oil is applied beneath it to place it on top of the support wafer and ensure thermal dissipation. (Fig.3 e))
- **Post-process**: After etching, the sample undergoes several cleaning steps. First, the thermal oil is carefully removed, then the sample is submerged in butanone for several hours. A solution of concentrated sulphuric acid and hydrogen peroxide is prepared for fine cleaning, followed up by an O_2 plasma process. (Fig.3 f))
- **HF etching**: This step is performed to remove the BOX under layer via hydrofluoric acid (HF) evaporation etching. (Fig.3 g))

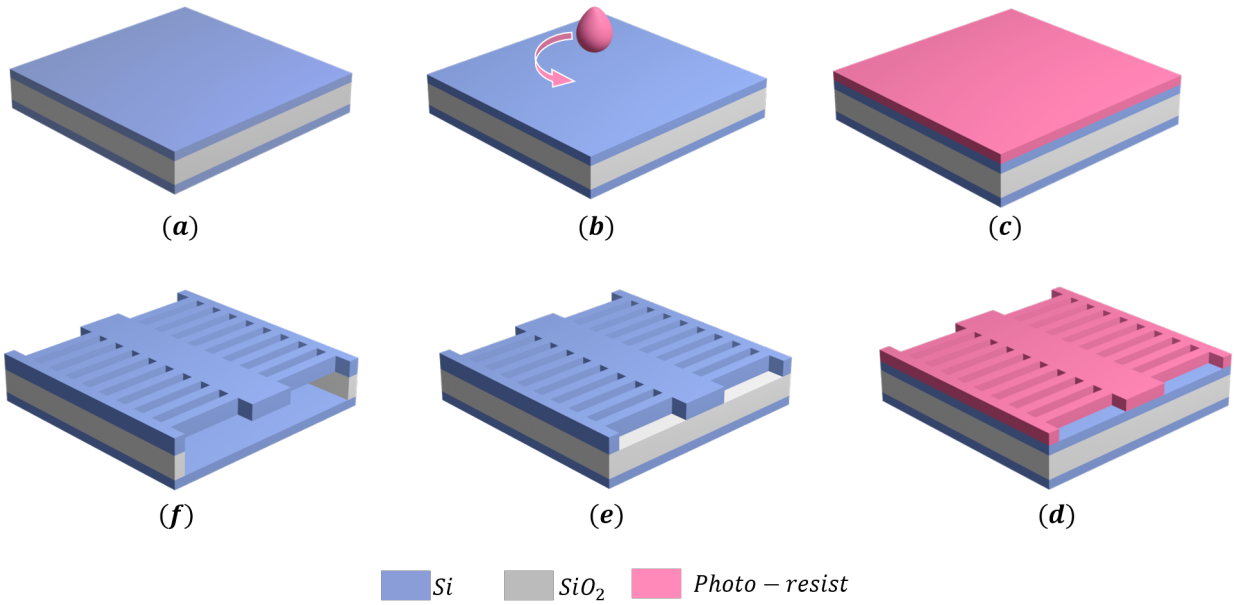

Figure 3.2 *Illustration of the steps followed in the fabrication of the SWG-suspended waveguides in C2N clean room.(a) SOI, (b) Spin coating, (c) E-beam lithography, (d) Developing, (e) Etching and cleaning and (f) HF etching.*

Figures 3.3 and 3.4 present scanning electron microscope (SEM) images of the SWG-cladded waveguides fabricated on a SOI wafer with a 700 nm silicon over-layer and a silicon dioxide bottom (BOX) cladding of 3 μm thickness.

The presented waveguides are not suspended (the liberation by HF etching in Figure 3.2 was not performed), in Figure 3.3 (a) one can observe the contrast between the silicon layer (darker top layer) and the silica BOX.

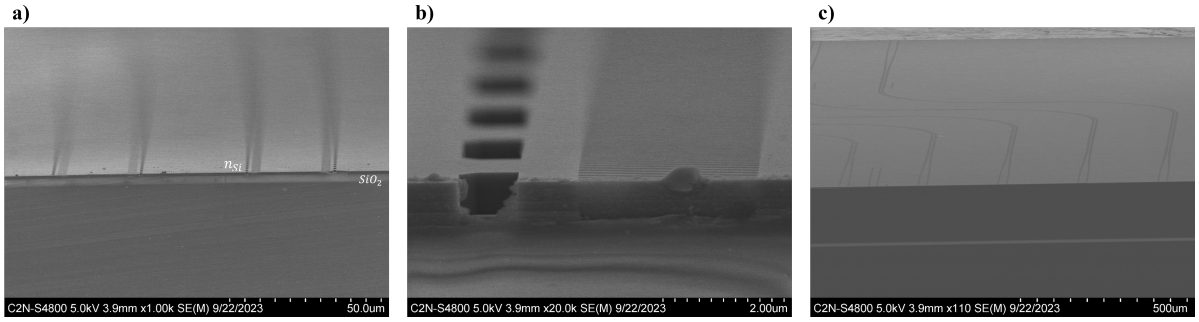

Figure 3.3 *Scanning electron microscope (SEM) images of the facet. Figure* ***a)*** *shows the contrast between the silicon and silica layers,* ***b)*** *presents a close up of the facet where the liberation holes and SWG-cladding of one side of the waveguide can be observed, and in* ***c)*** *a general visualization of the waveguides is shown.*

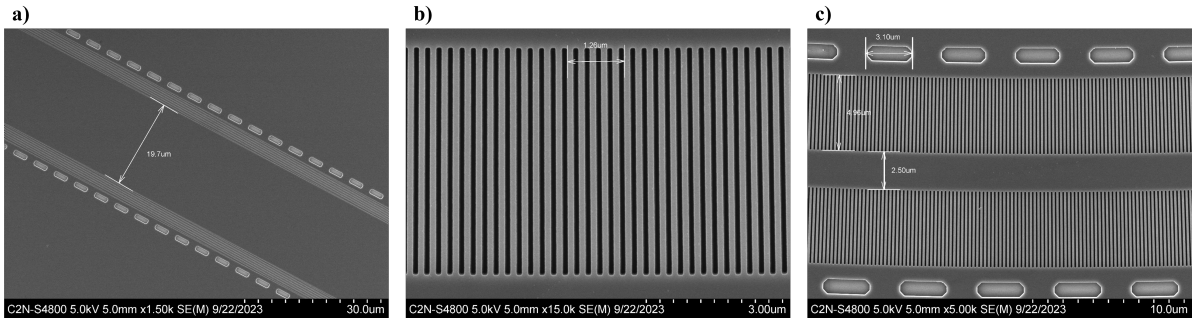

Figure 3.4 *SEM images of the SWG-cladded waveguides.* ***a)****SWG-cladded taper with width of 20 µm,****b)*** *SWG structure showing 5 periods with Λ=250 nm ,and* ***c)*** *SWG-cladded waveguide with* W_{core} *= 2.5 µm.*

3.3 Experimental characterization

The characterization of the SWG-cladded waveguides was carried out in the mid-IR experimental room at C2N.

Set-up description

A schematic of the employed mid-infrared setup is presented in Figure 3.5. It is composed of a tunable mid-IR laser (MIRcat, Daylight solutions) containing four different quantum cascade laser (QCL) modules. The wavelength ranges for the QCL modules are as follows: the first QCL module covers wavelengths from 5.08 μm to 6.16 μm, the second one from 5.76 μm to 7.04 μm, the third one from 7.02 μm to 8.97 μm, and the fourth QCL comprise the wavelengths from 8.11 μm to 11.21 μm.

The QCL laser outputs in transverse magnetic (TM) polarization; therefore, a polarization rotator is used to obtain transverse electric (TE) polarization. Light is both coupled to and collected from the sample using aspherical lenses. After recollection, it is directed towards an external mercury cadmium telluride (MCT) photodetector (DSS-MTC(14)-020, Horiba). The MCT is cooled with liquid nitrogen to minimize thermal noise.

The near-infrared and mid-infrared cameras are use for alignment. The first one allows the visualization of light transmission through the waveguides and optimization of the input and output lens positions. The MIR camera is used to visualize the mode coupled to the structure.

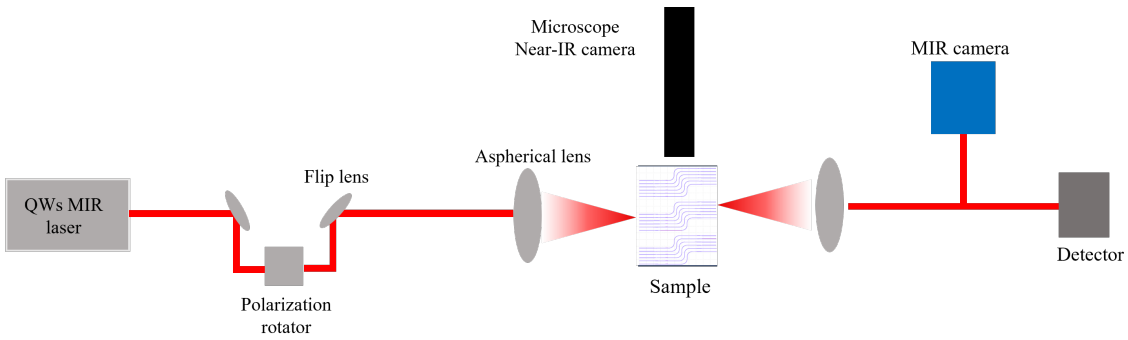

Figure 3.5 *Diagram illustrating the mid-IR setup used for sample characterization.It is composed by a multiple QW laser, a polarization rotator, aspherical lenses for coupling, near- and mid-infrared cameras and a mid-IR MCT detector.*

Results

Figure 3.6 presents preliminary measurements of the transmission spectra of the SWG-cladded waveguides with silica under cladding for the systems with period Λ of 250 nm and duty cycle DC of 0.6. The envelope transmission due to laser response is highly noticeable.

The samples were characterized in a wavelength range from 5 to 9 μm with a sampling step of 1 nm. The set-up comprises almost 1 m of free space propagation, therefore the measured spectra presents sharp dips due to atmospheric absorption.

In the measurements, we can observe that the transmission considerably diminishes, mainly due to silicon absorption and weak light confinement, starting from 7 μm wavelength. To analyse the system using methods like the cut-back method and to obtain devices properties such as the losses, we will need to perform additional measurements on SWG-cladded waveguides with varying lengths.

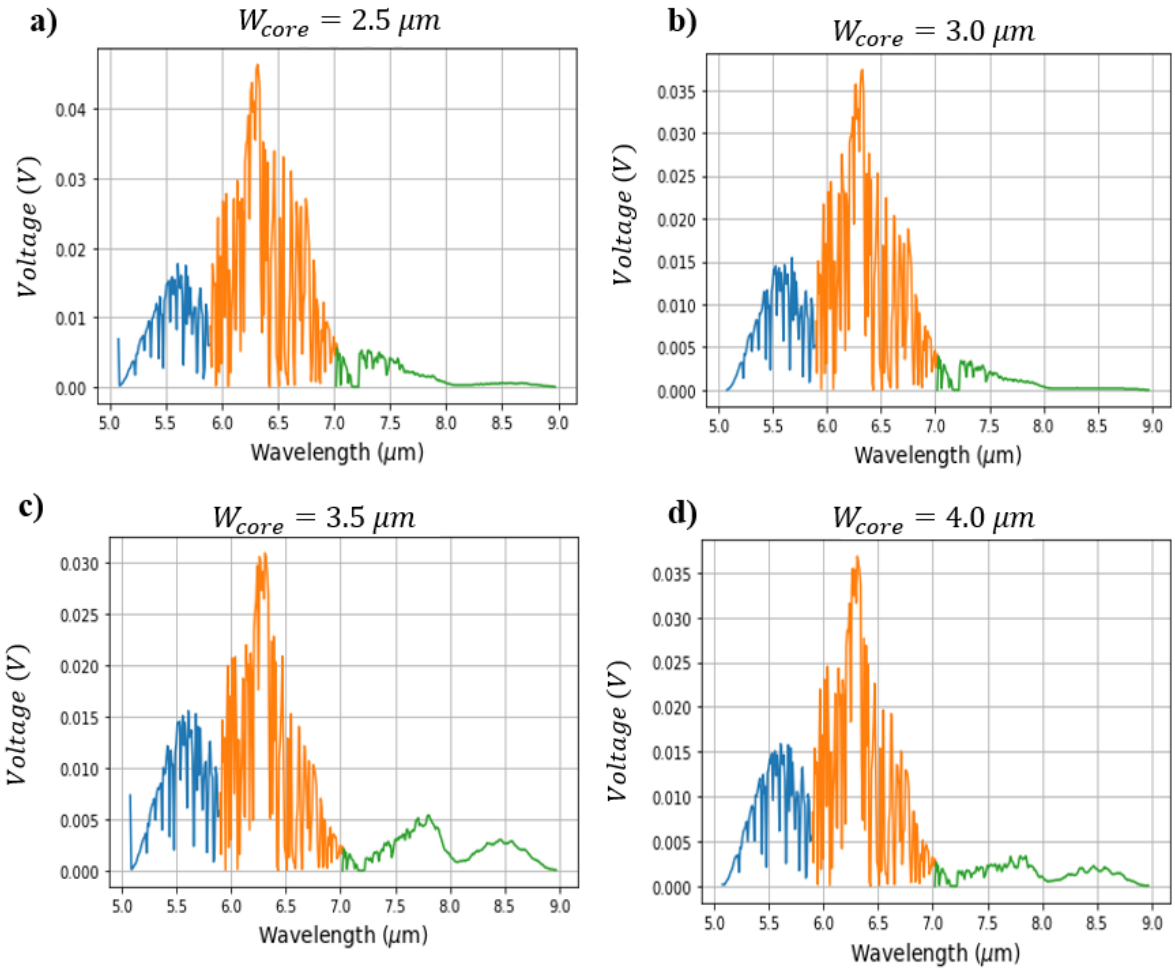

Figure 3.6 *Preliminary transmission measurements of the SWG-cladded waveguides with duty cycle of 0.6 with:* ***a)*** W_{core}*=2.5 µm,* ***b)*** W_{core}*=3.0 µm,* ***c)*** W_{core}*=3.5 µm, and* ***d)*** W_{core}*=4.0 µm, conducted in a wavelength range from 5 to 9 µm.*

3.4 Summary

In this chapter, we presented the design of SWG-cladded waveguides and the fabrication process employed for their production. We fabricated samples measuring 0.5 cm × 1 cm in size, which contained SWG-cladded waveguides with varying core widths and duty cycles on a wafer with 700 nm Si thickness, ensuring balance between mode confinement and etching process.

These samples were characterized within a wavelength range spanning from 5 to 7 μm. In all cases, we obtained transmission spectra in which the laser envelope is observable, with peaks marked by atmospheric absorption. The transmission spectra exhibited the expected silicon absorption beginning at 7 μm. For further studies, we plan to fabricate waveguides with varying lengths, cores and duty cycles, and conduct characterizations to extract device properties, including loses.

The next step for the fabricated samples involves liberating them from the silica

under cladding through hydrofluoric acid etching. Additionally, calibration measurements will be performed to remove effects of laser envelope and atmospheric absorption. Further studies will also be necessary to optimize the bends and reduce losses while achieving more compact devices.

4 Supercontinuum generation

Supercontinuum generation (SCG) has been widely studied for the development of mid-IR light sources, finding various applications in areas such as spectroscopy, optical telecommunications, and light sources. This is due to the fact that it enables light emission over an ultrawide spectral range within a single photonic device.

The first section of this chapter presents the working principle of supercontinuum generation (SCG). In section 2, we introduce two different methods for dispersion calculation. The first method is base on the effective index method using FDM simulations, while the second one exploits the relation between group velocity dispersion (GVD) and bandstructure. Simulations of SCG based on FDM dispersion results are also presented.

4.1 Introduction

The development of supercontinuum (SC) light sources has grown significantly in the past years due to their relevance in multiple applications requiring a broad-spectrum coverage. For example, in spectroscopy, SCG can be used as a broadband light source for absorption spectroscopy, in which the bandwidth of the supercontinuum determines the range of chemical species that can be identified.

In optical telecommunications, SCG can be used for wavelength division multiplexing, since it is an efficient way to generate broadband frequency combs with a spectral range determined by the source's repetition rate (Lafforgue et al. 2022).

This sources can also be applied to imaging techniques that require broadband sources, such as optical coherence tomography (OCT) where the bandwidth of the pulse determines the imaging performance. A broader spectrum means more sensitive and higher resolution imaging technique.

Broadband supercontinuum generation in mid-IR have been demonstrated in different platforms, such as in SOI (Wei et al. 2020), chalcogenide glasses (Y. Yu et al. 2016), silicon on sapphire and suspended silicon.

Ge and GeSi have also been implemented to further extend SCG into the mid-IR, as shown by Della Torre et al. (2021). The authors achieved the generation of a supercontinuum on a germanium-on-silicon waveguide spanning almost one octave, covering from 3 μm to 5 μm.

As mentioned before, silicon presents favourable properties for SCG in mid-IR, such as high non-linear coefficient and negligible two-photon absorption. Additionally, the high index contrast provides tight optical confinement. Recently, Thi-Thuy

(2022) demonstrated the generation of a supercontinuum expanding over 2.35 octaves between 1.5 and 7.5 μm wavelength using SWG-cladded suspended silicon structures.

4.1.1 Principle of supercontinuum generation

A supercontinuum is a broad, continuous spectrum of light generated by an intense narrowband pulse light source interacting non-linearly with the propagation medium.It involves the interaction between nonlinear and linear effects. Two key principles that play a crucial point in its generation are Group Velocity Dispersion (GVD) and Self-Phase Modulation (SPM).

Self-phase modulation

Self-phase modulation is a non-linear effect, a consequence of the interaction of an intense optical field and the bound electrons of a dielectric medium, which gives rise to changes in the frequency and phase of the optical field during its propagation.

When a high intensity pulse propagates through a media, the refractive index n becomes intensity dependent(Agrawal 2013),

$$n = n_0 + n_2 I, \tag{4.1}$$

where n_0 is the linear refractive index, n_2 is the Kerr refractive index, and I is the intensity of the electric field. The variation of the refractive index induces a phase shift in the pulse, leading to the self phase modulation (SPM) phenomenon.

At higher intensity, the refractive index is higher, causing the carrier wave to travel more slowly, while the tails of the envelope travel faster. In most materials, $n_2 > 0$ (Lafforgue et al. 2022), leading to a positive chirp.

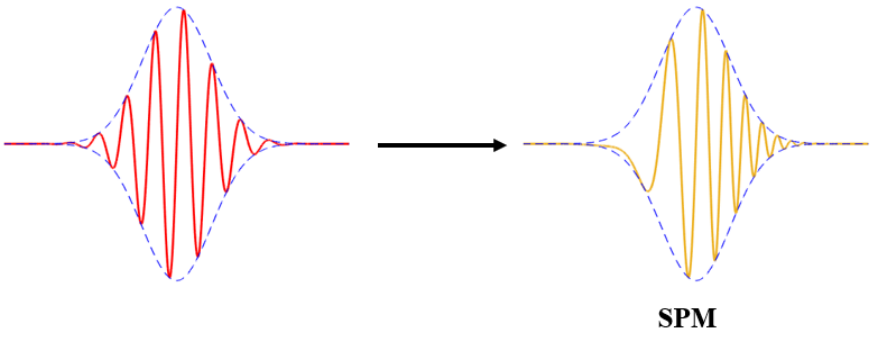

Figure 4.1 *Schematic representation of the self phase modulation effect on an optical pulse.*

The propagation length for which the nonlinear effects of SPM became relevant

is given by,

$$L_{\mathbf{NL}} = \frac{1}{\gamma P_0}, \tag{4.2}$$

where γ is the nonlinear coefficient and P_0 is the input power. $\mathrm{L_{NL}}$ corresponds to the length at which the pulse accumulates a phase shift of 1 rad.

The nonlinear coefficient γ is computed from the effective mode area $\mathrm{A_{eff}}$ and the Kerr coefficient $\mathrm{n_2}$ through,

$$\gamma = \frac{\omega_0 n_2}{c A_{\mathrm{eff}}(\omega_0)}, \tag{4.3}$$

where ω_0 is the central frequency, $\mathrm{n_2}$ the non-linear index and $\mathrm{A_{eff}}$ the effective modal area.

$$A_{\mathrm{eff}} = \frac{(\int_S |E^2|)^2}{\int_S |E^4|}, \tag{4.4}$$

where S is the waveguide cross-section and E the electric field.

Group velocity dispersion

When a pulse propagates along a waveguide, it is affected by the dispersion, meaning that at a given distance ($\mathrm{L_D}$), each frequency component of the original pulse will travel with a different delay with respect to the central frequency (ω_0). In the temporal domain, the pulse peak power will decrease meanwhile its duration increases during propagation (Lafforgue et al. 2022).

The group velocity dispersion (GVD) β_2 is defined in therms of the coefficients associated to the Taylor expansion of the propagation constant $\beta(\omega)$ around the frequency ω_0:

$$\beta(\omega) = \sum_{k=0}^{\infty} \frac{\beta_k}{k!}(\omega - \omega_0)^k, \tag{4.5}$$

where β_k are the higher order dispersion coefficients given by:

$$\beta_k = \frac{\partial^k \beta}{\partial \omega^k}. \tag{4.6}$$

β_0 is the wave number at the central frequency ω_0, β_1 is related to the group velocity v_g through $\beta_1 = \frac{1}{v_g}$ where v_g and β_2 is the group velocity dispersion (GVD) with units of $\mathrm{s^2\ m^{-1}}$. The GVD is often described by the dispersion parameter D = - $\omega_0^2 \beta_2$ /(2π c), with units of $\mathrm{ps\ nm^{-1}\ km^{-1}}$. Based on the sign of the dispersion, two different regimes are possible (see Figure 4.2):

- the normal dispersion regime occurs when $\beta_2 > 0$ (D < 0), indicating that

longer wavelengths travel faster than shorter wavelengths.

- the anomalous dispersion occurs when $\beta_2 < 0$ (D > 0), indicating that shorter wavelengths travel faster than longer wavelengths.

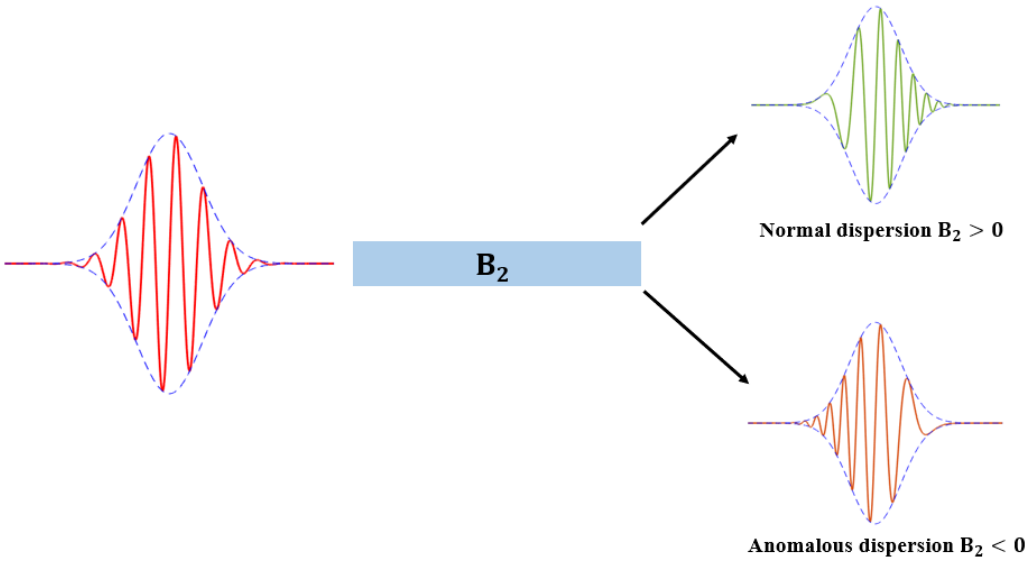

Figure 4.2 *Schematic representation of a pulse propagating through a medium with: normal dispersion ($\beta_2 > 0$) which induces a positive chirp and anomalous dispersion ($\beta_2 < 0$) which results in a negative chirp.*

The characteristic length for which the effects of dispersion became relevant is given by,

$$L_D = \frac{T_0^2}{|\beta_2|}, \tag{4.7}$$

where T_0 is the initial pulse duration. It corresponds to the distance at which a Gaussian optical pulse undergoes a temporal broadening of a factor of $\sqrt{2}$.

In the normal dispersion regime, the evolution of the phase is the same as in SPM (both have positive chirp), meanwhile in anomalous dispersion regime SPM and GVD have opposite consequences.

Solitons and soliton fission

Soliton dynamics play an essential role in supercontinuum generation using femtosecond pump pulses.In the anomalous dispersion regime ($\beta_2 < 0$), the nonlinear chirp from SPM (positive) and the linear chirp from GVD (negative) can counterbalance each other. When SPM and GVD perfectly balance each other ($L_D = L_{NL}$), the initial pulse propagates unperturbed and is referred to as "soliton". The fundamental soliton is described by N = 1, higher order solitons can exist under the condition:

$$N^2 = \frac{L_D}{L_{NL}} = \frac{\gamma P_0 T_0^2}{|\beta_2|}, \tag{4.8}$$

where N^2 is the soliton order, $\mathrm{L_D}$ is the dispersion length, L_{NL} is the non-linear length, $\mathrm{T_0}$ is the initial pulse duration, and $\mathrm{P_0}$ the peak power.

Without other nonlinear effects than SPM or high-order dispersions, the generation of supercontinuum is not possible. However, it is important to notice that high-order solitons (N » 1) are sensitive to perturbations. The process in which a high-order soliton breaks up into a series of N fundamental solitons is known as soliton fission (see Figure 4.3), and it covers a higher bandwidth than the original pulse.

The distance in which fission occurs generally corresponds to the point where the evolving input pulse soliton reaches its maximum bandwidth: $L_{\mathrm{fiss}} = L_{\mathrm{D}}/N$. The most commons perturbations responsible for soliton fission include self-stepping effect, stimulated Raman scattering (SRS), and high order dispersions.

For supercontinuum generation, a critical parameter is the wavelength at which β_2 or D become zero. This is known as the zero dispersion wavelength (ZDW) and it separates the normal dispersion region ($\mathrm{D} < 0$) and the anomalous dispersion region ($\mathrm{D} > 0$).

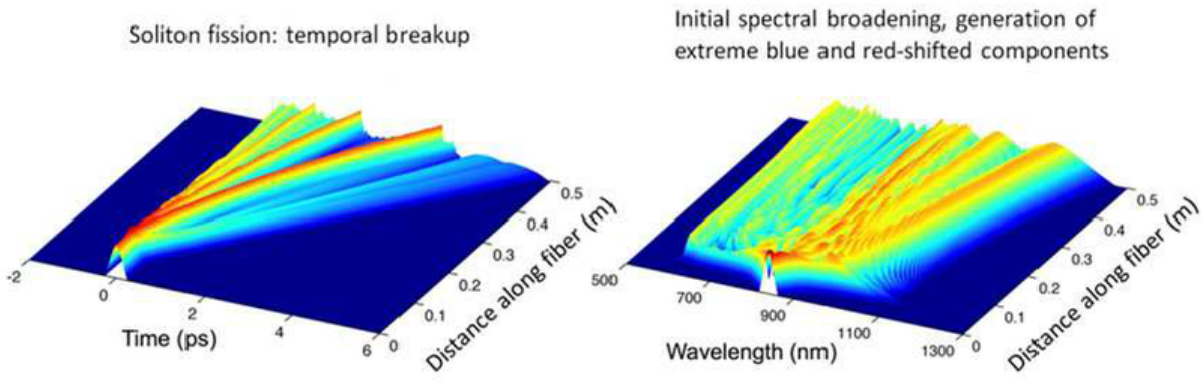

Figure 4.3 *Numerical simulations of soliton fission and supercontinuum generation on fibre, presented on Dudley and Genty 2013.*

Besides soliton fission, there are other effects that can contribute to the generation of additional bandwidth. When high order dispersion is present, a soliton propagating near zero dispersion wavelength (ZDW) can transfer a portion of its energy to the normal group velocity dispersion (GVD) regime, where the group velocity decreases as optical frequencies increase. This process generate a "dispersive wave" also known as "non-soliton radiation" or "Cherenkov radiation" (Skryabin and Gorbach 2010). Furthermore, even when perturbed by dispersive wave generation, solitons can experience a shift towards longer wavelengths due to soliton

self-frequency shift.

4.2 Dispersion computation

The dispersion of the waveguides was determined through Finite-Difference Method (FDM) and by using the bandstructure results obtained from the full vectorial 3D-FDTD simulations.

Let's recall the system analysed in Section 2.2.2, where the SWG-cladding was replaced by a homogeneous medium with effective refractive index, denoted as n_{clad} obtained through Rytov's equations (Eq. 2.2). Using FDM simulations, we were able to compute the effective index for a selected mode. In this part of the study, we used the same system approximation and simulation setup to determine the dispersion D, β_2, and the effective area for various suspended SWG-cladded waveguide geometries.

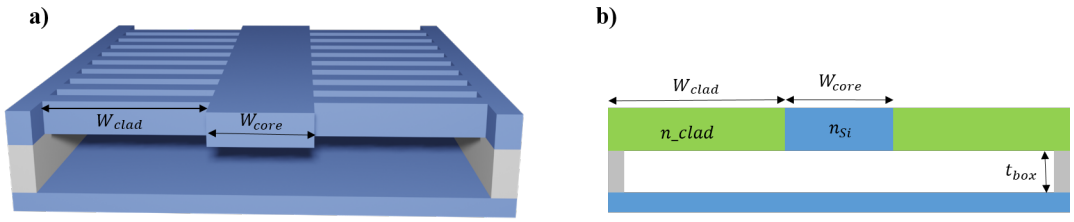

Figure 4.4 *a)Illustration of a SWG-suspended waveguide and* ***b)****cross-section of the waveguide with equivalent refractive index* n_{clad}.

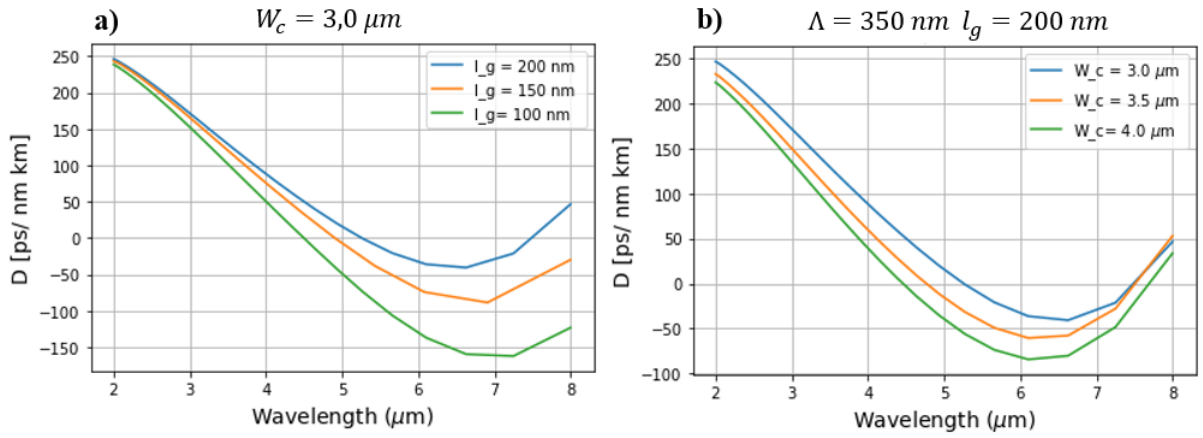

Figure 4.5 *Comparison of the dispersion calculated using FDM for:* ***a)*** *Multiple duty cycles with* l_g = *100, 150 and 200 nm and a fixed core width of 3.0 μm, and* ***b)*** *Core widths* W_{core} = *3.0, 3.5 and 4.0 μm with a duty cycle (DC =* a/Λ*) of 0.43.*

In Figure 4.5 we present a comparison of the obtained dispersion (D) for multiple

cores and duty cycles. In all the cases, anomalous dispersion regime (D > 0) is observed for wavelengths shorter than 4.5 μm.

To calculate the dispersion using the bandstructure results obtained through 3D-FDTD simulations, we exploited the relation between the group velocity dispersion (GVD) and the bandstructure:

$$D = \frac{c}{v_g^2 \lambda^2} \frac{\partial v_g}{\partial f}, \tag{4.9}$$

where c is the light velocity, λ the wavelength, and v_g the group velocity given by $v_g = 2\pi \partial f / \partial k$ where f the frequency and k the wavevector.

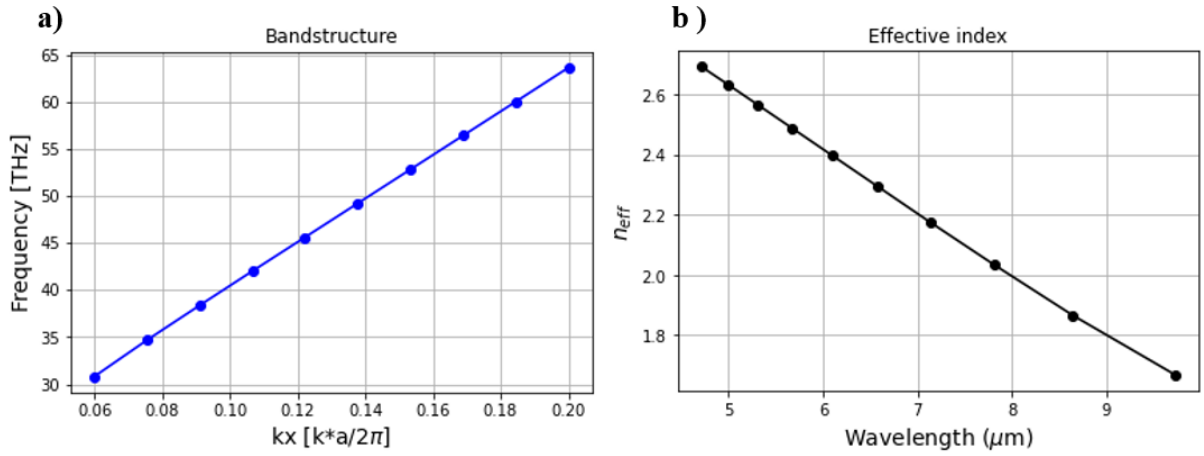

Figure 4.6 a) *Calculated bandstructure using 3D-FDTD of the suspended SWG-cladded waveguide with geometrical parameters: Λ = 350 nm, W_{clad} = 5 μm, W_{core} = 3.0 μm, DC = 0.43 and silicon thickness t = 700 nm.* ***b)*** *Calculated effective index as function of the wavelength using Eq. 2.6.*

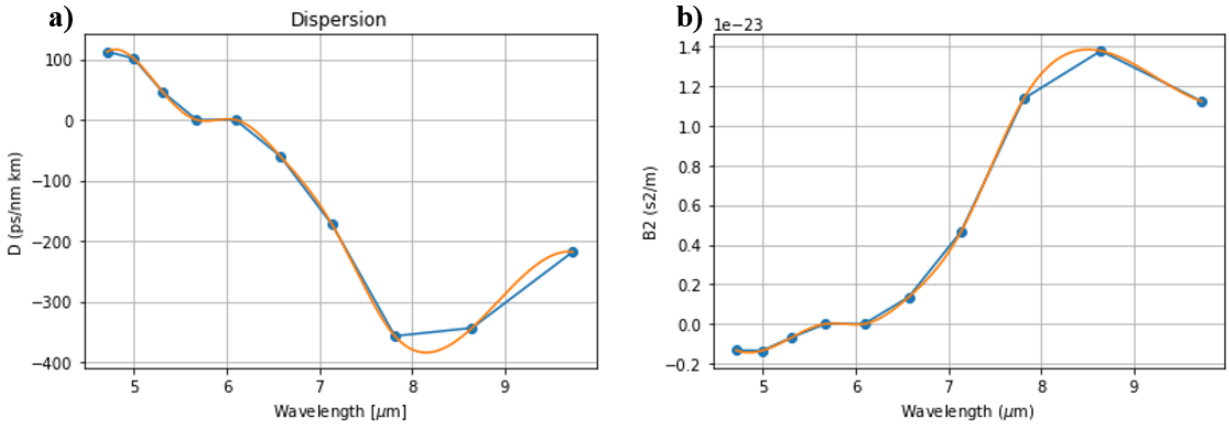

Figure 4.7 *Dispersion computed from the bandstructure using Eq. 4.9 for the suspended SWG-cladded waveguide with geometrical parameters: Λ = 350 nm, W_{clad} = 5 μm, W_{core} = 3.0 μm, DC = 0.43 and silicon thickness t = 700 nm.*

Figure 4.7 presents dispersion of the system with W_{core} = 3.0 μm and DC = 0.43 computed using the bandstructure data shown in Figure 4.6 and equation 4.9. The presented results significantly differ from those computed through FDM, a difference was expected due to FDM approximations. Nevertheless, further studies need to be carried out for a better understanding and interpretation of the data.

4.3 Supercontinuum simulations

The supercontinuum generation in the SWG-cladded waveguide can be modelled by solving the generalized nonlinear Schrödinger equation (GNLSE) (Skryabin and Gorbach 2010):

$$\frac{\partial A}{\partial z}+\frac{\alpha}{2}A-\sum_{k\geq 2}\frac{i^{k+1}}{k!}\beta_k\frac{\partial^k A}{\partial T^k}=i\gamma(1+i\tau_{shock}\frac{\partial}{\partial T})\times(A(z,T)\int_{-\infty}^{\infty}R(T')|A(z,T-T')|^2dT'). \tag{4.10}$$

The left-hand side of the equation models the linear effects where A is the pulse temporal envelope, α the propagation loss and β_k the dispersion coefficients (Eq. 4.5). The right-hand side models the nonlinear effects, here τ_{shock} describes the first-order frequency dependence of the modal area and the self-steepening effect. $R(t)$ is the Raman response function (Agrawal 2013), γ is the non-linear coefficient given by Eq. 4.3, and z is the propagation distance.

The numerical simulation of SCG on the suspended waveguides was performed using the MATLAB codes proposed by Skryabin and Gorbach 2010 (see App. 5). Where include the dispersion of the nonlinear response is to describe it directly in frequency domain, the generalised NLSW for the pulse evolution writes as

$$\frac{\partial A}{\partial z}=i\frac{\gamma\omega}{\omega_0}exp(-\hat{L}z)\mathcal{F}\left[A(z,T)\int_{-\infty}^{\infty}R(T')|A(z,T-T')|^2dT'\right] \tag{4.11}$$

which is obtained by ignoring the frequency dependence of n_2, n_{eff} and A_{eff}. In this equation the A(z, T) field is integrated in the frequency domain. $\hat{L}$ is the linear operator, given by $\hat{L}$ = i($\beta(\omega)-\beta(\omega_0)-\beta_1(\omega_0)[\omega-\omega_0])-\alpha(\omega)/2$.

For the numerical simulation, we considered a pump pulse with a quadratic hyperbolic shape in time domain, with a 220 fs duration and a 1 MHz repetition rate. The pump wavelength was taken as 3.53 μm, and the peak power (P_0) was 1 kW. The nonlinear index coefficient of silicon n_2, was considered as 2.5 $\times$ 10^{-18}, and the propagation distance z was set to 4 mm. The number of grid points is 2 $\times$ 10^{13} and the width of the time window is considered as 12.5 $\times$ 10^{-12} s. In this simulation the Raman response, the self steepening effect and the losses were not

considered.

In order to compute the non-linear coefficient γ, the effective area A_{eff} and dispersion β_2 were obtained using FDM simulations. In Figure 2.10 a), the effective area is plotted against wavelength for the fundamental TE mode in a system with a duty cycle of 0.43 and several core widths.

The effective area varies due to the wavelength dependence of the refractive index, affecting the nonlinear effects responsible for supercontinuum generation. These effects are strongly dependent on the local field strength. In the figure, one can observe that at longer wavelengths, the effective area increases, leading to a reduction in nonlinear effects.

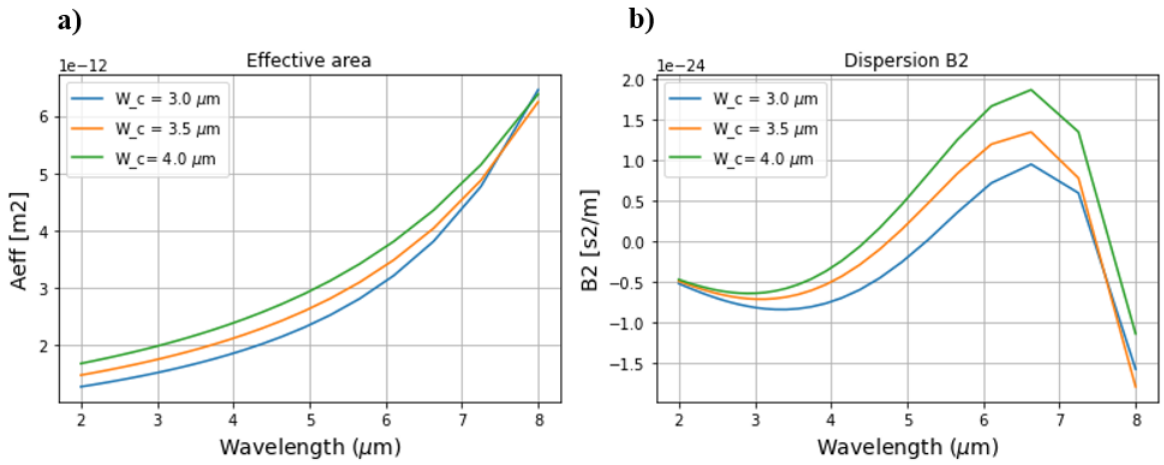

Figure 4.8 *Results for the system with duty cycle (DC) of 0.43 and several cores of the* ***a)*** *effective area, and* ***b)*** *dispersion β_2 with respect to the wavelength computed using 2D FDM effective index simulations.*

Figure 4.9 shows the evolution of the pulse in spectral (a) and temporal domain (b) while it propagates through the SWG-cladded suspended waveguide. In the image, we can observe a broadening between 2.5 and 4.5 μm wavelength.

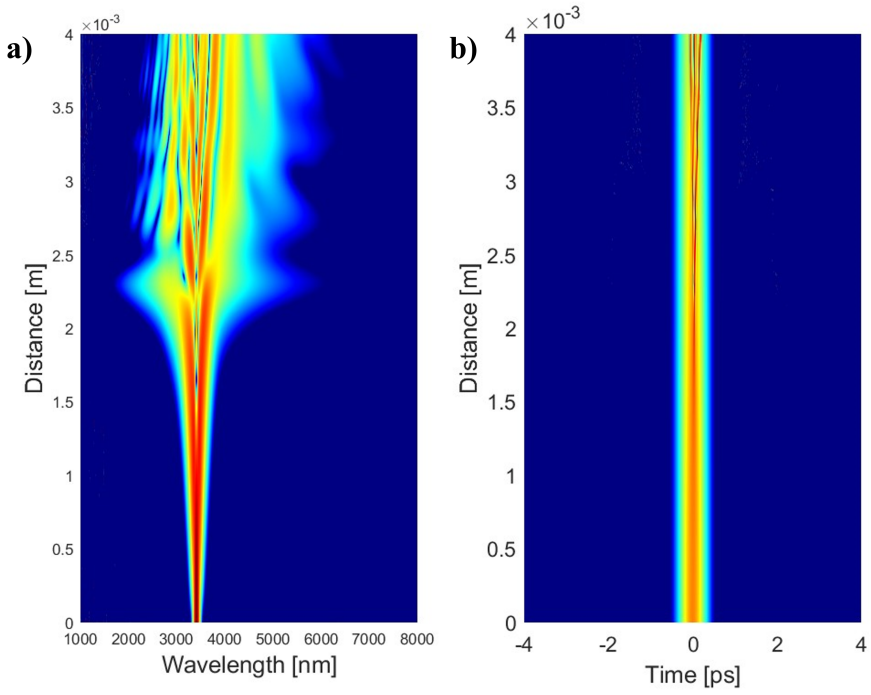

Figure 4.9 *MATLAB simulation of a pulse evolution in a SWG-cladded suspended silicon waveguide with* W_{core} *= 3 µm and duty cycle of 0.43. With a pump peak power of 1 kW and 3.4 µm wavelength.Figure* ***a)*** *is the evolution in spectral and* ***b)*** *in temporal domain.*

4.4 Summary

In this chapter, we have introduced the concept of supercontinuum generation and delved into the physical phenomena that contribute to it, including linear effects such as Group Velocity Dispersion (GVD), and non-linear effects like Self-Phase Modulation (SPM), soliton generation and soliton fission.

We presented the outcomes of dispersion calculations through Finite Difference Method (FDM) simulation for various waveguide cores and duty cycles, as well as through 3D-FDTD bandstructure simulations for a system characterized by a W_{core} = 3.0 μm and DC = 0.43. It is important to notices that further studies need to be carried out for a better understanding and interpretation of the data.

Numerical supercontinuum simulations were conducted for an idealized system devoid of losses, which has revealed small spectrum broadening effect between wavelengths of 2.5 and 4.5 μm. This opens a door to additional investigations and refinements aimed at supercontinuum generation in optical waveguides as a means to produce mid-IR light sources.

5 Conclusions

In this work, I presented the initial studies for the design and development of silicon metamaterial waveguides working in the mid-IR range. The use of SWG suspended silicon platforms offer a solution to deal with the silica absorption in mid-IR, while at the same time granting freedom to tailor light propagation in SiP devices.

In the analysis of the SWG-cladded suspended silicon waveguides, I employed two main simulation methods: the Finite Difference Method (FDM) and the full vectorial 3D Finite Difference Time Domain (FDTD). These methods allowed me to gain a comprehensive understanding of the behaviour of the SWG-cladded suspended waveguide in the Mid-IR range.

In the FDM simulations, I approximated the SWG cladding as a homogeneous medium by defining an effective index, denoted as n_{cladd}. This approach enabled a simplified representation of the cladding while still giving a good approximation of its effective refractive index, dispersion, and mode effective area.

On the other hand, the full vectorial 3D FDTD simulations offered a more detailed analysis. This method allowed me to treat the system as a periodic structure, applying Bloch boundary conditions at the direction of propagation.By doing so, I could obtain the bandstructure, effective refractive index and dispersion of the systems.Throughout these simulations, I explored how variations in core width and duty cycle influenced these critical optical properties.

I designed a set of SWG-cladded waveguides with various geometries and participated in their fabrication. However, the samples were not liberated (i.e., the silica cladding was not removed) due to cleanroom timings constraints. Nevertheless, I characterized the transmission of the samples using the mid-IR setup in a wavelength range from 5 to 9 μm. For all cases, I obtained transmission spectra in which the laser envelope is observable, as well as sharp deeps due to atmospheric absorption.The transmission spectra diminish at 7 μm wavelength due to silicon absorption and weak light confinement.

Finally, I have shown the supercontinuum numerical modelling for an ideal system based on the FDM simulations results with a core width of 3.0 μm and duty cycle of 0.43, in which a small spectrum broadening effect between wavelengths of 2.5 and 4.5 μm was observed.

In the short-term goal, waveguides with varying lengths, cores and duty cycles, will be fabricated and characterized to extract device properties, including loses. The next step for the fabricated samples involves liberating them from the silica under cladding through hydrofluoric acid etching. Afterward, the samples will be pumped with a femtosecond laser to study nonlinearities.

Deeper investigations of how to extend Si components library towards longer wavelengths, engineering suspended SWG Si membranes to fully benefit from Si transparency and integrating RE-doped ChG materials will be further developed in my PhD studies.

References

Agrawal, Govind P (2013). *Nonlinear Fiber Optics (5th Edition)*. eng. Optics and Photonics. San Diego: Elsevier. ISBN: 9780123970237.

Bjelajac, A. et al. (Jan. 2022). "Up to 300 K lasing with GeSn-On-Insulator microdisk resonators". In: *Opt. Express* 30.3, pp. 3954–3961. DOI: 10.1364/OE.449895. URL: https://opg.optica.org/oe/abstract.cfm?URI=oe-30-3-3954.

Bock, Przemek J. et al. (Sept. 2010). "Subwavelength grating periodic structures in silicon-on-insulator: a new type of microphotonic waveguide". In: *Opt. Express* 18.19, pp. 20251–20262. DOI: 10.1364/OE.18.020251. URL: https://opg.optica.org/oe/abstract.cfm?URI=oe-18-19-20251.

Bodiou, Loïc et al. (2018). "Mid-infrared guided photoluminescence from integrated Pr3+-doped selenide ridge waveguides". In: *Optical Materials* 75, pp. 109–115. ISSN: 0925-3467. DOI: https://doi.org/10.1016/j.optmat.2017.10.001. URL: https://www.sciencedirect.com/science/article/pii/S0925346717306146.

Carlie, Nathan et al. (Dec. 2010). "Integrated chalcogenide waveguide resonators for mid-IR sensing: leveraging material properties to meet fabrication challenges". In: *Opt. Express* 18.25, pp. 26728–26743. DOI: 10.1364/OE.18.026728. URL: https://opg.optica.org/oe/abstract.cfm?URI=oe-18-25-26728.

Chang, Yu-Chi et al. (July 2012). "Low-loss germanium strip waveguides on silicon for the mid-infrared". In: *Opt. Lett.* 37.14, pp. 2883–2885. DOI: 10.1364/OL.37.002883. URL: https://opg.optica.org/ol/abstract.cfm?URI=ol-37-14-2883.

Cheben, P. et al. (May 2006). "Subwavelength waveguide grating for mode conversion and light coupling in integrated optics". In: *Opt. Express* 14.11, pp. 4695–4702. DOI: 10.1364/OE.14.004695. URL: https://opg.optica.org/oe/abstract.cfm?URI=oe-14-11-4695.

Cheng, Zhenzhou et al. (2012). "Mid-infrared Suspended Membrane Waveguide and Ring Resonator on Silicon-on-Insulator". In: *IEEE Photonics Journal* 4.5, pp. 1510–1519. DOI: 10.1109/JPHOT.2012.2210700.

Chrétien, Jérémie et al. (Oct. 2019). "GeSn Lasers Covering a Wide Wavelength Range Thanks to Uniaxial Tensile Strain". In: *ACS Photonics* 6.10, pp. 2462–2469. DOI: 10.1021/acsphotonics.9b00712. URL: https://doi.org/10.1021/acsphotonics.9b00712.

Coutard, J. G. et al. (Apr. 2020). "Volume Fabrication of Quantum Cascade Lasers on 200 mm-CMOS pilot line". In: *Scientific Reports* 10.1, p. 6185. ISSN: 2045-2322. DOI: 10.1038/s41598-020-63106-4. URL: https://doi.org/10.1038/s41598-020-63106-4.

Della Torre, Alberto et al. (Jan. 2021). "Mid-infrared supercontinuum generation in a low-loss germanium-on-silicon waveguide". In: *APL Photonics* 6.1, p. 016102. ISSN: 2378-0967. DOI: 10.1063/5.0033070. eprint: https://pubs.aip.org/aip/app/article-pdf/doi/10.1063/5.0033070/14571086/016102_1_online.pdf. URL: https://doi.org/10.1063/5.0033070.

Dudley, John and G. Genty (June 2013). "Supercontinuum light". In: *Physics Today* 66. DOI: 10.1063/PT.3.2045.

Faist, Jerome et al. (Apr. 1994). "Quantum cascade laser". English. In: *Science* 264.5158. Copyright - Copyright American Association for the Advancement of Science Apr 22, 1994; Last updated - 2023-07-10; CODEN - SCIEAS, p. 553. URL: https://libproxy.tuni.fi/login?qurl=https%3A%2F%2Fwww.proquest.com%2Fscholarly-journals%2Fquantum-cascade-laser%2Fdocview%2F213555454%2Fse-2%3Faccountid%3D14242.

Gonzales, David (Jan. 2020). "Sub-wavelength metamaterials for high-performance photonic microdevices". PhD thesis. Universidad Complutense de Madrid.

Gutierrez-Arroyo, Aldo et al. (Oct. 2016). "Optical characterization at 7.7 µm of an integrated platform based on chalcogenide waveguides for sensing applications in the mid-infrared". In: *Opt. Express* 24.20, pp. 23109–23117. DOI: 10.1364/OE.24.023109. URL: https://opg.optica.org/oe/abstract.cfm?URI=oe-24-20-23109.

Halir, Robert, Przemek Bock, et al. (Sept. 2014). "Waveguide sub-wavelength structures: A review of principles and applications". In: *Laser Photonics Reviews* 9. DOI: 10.1002/lpor.201400083.

Halir, Robert, Pavel Cheben, et al. (Nov. 2016). "Ultra-broadband nanophotonic beamsplitter using an anisotropic sub-wavelength metamaterial: Ultra-broadband nanophotonic beamsplitter…" In: *Laser Photonics Reviews* 10, pp. 1039–1046. DOI: 10.1002/lpor.201600213.

Hendriks, Ward et al. (Jan. 2021). "Rare-earth ion doped Al 2 O 3 for active integrated photonics". In: *Advances in Physics: X* 6, p. 1833753. DOI: 10.1080/23746149.2020.1833753.

J. Soler Penades, Jordi et al. (Oct. 2014). "Suspended SOI waveguide with sub-wavelength grating cladding for mid-infrared". In: *Optics Letters* 39. DOI: 10.1364/OL.39.005661.

Kang, Jian, Mitsuru Takenaka, and Shinichi Takagi (May 2016). "Novel Ge waveguide platform on Ge-on-insulator wafer for mid-infrared photonic integrated circuits". In: *Opt. Express* 24.11, pp. 11855–11864. DOI: 10.1364/OE.24.011855. URL: https://opg.optica.org/oe/abstract.cfm?URI=oe-24-11-11855.

Kou, Rai et al. (Mar. 2018). "Mid-IR broadband supercontinuum generation from a suspended silicon waveguide". In: *Opt. Lett.* 43.6, pp. 1387–1390. DOI: 10.1364/

OL.43.001387. URL: https://opg.optica.org/ol/abstract.cfm?URI=ol-43-6-1387.

Lafforgue, Christian et al. (Mar. 2022). "Supercontinuum generation in silicon photonics platforms". In: *Photon. Res.* 10.3, A43–A56. DOI: 10.1364/PRJ.445304. URL: https://opg.optica.org/prj/abstract.cfm?URI=prj-10-3-A43.

Li, Nanxi et al. (Feb. 2018). "Broadband 2-µm emission on silicon chips: monolithically integrated Holmium lasers". In: *Opt. Express* 26.3, pp. 2220–2230. DOI: 10.1364/OE.26.002220. URL: https://opg.optica.org/oe/abstract.cfm?URI=oe-26-3-2220.

Li, Wei et al. (Dec. 2016). "Germanium-on-silicon nitride waveguides for mid-infrared integrated photonics". In: *Applied Physics Letters* 109.24, p. 241101. ISSN: 0003-6951. DOI: 10.1063/1.4972183. eprint: https://pubs.aip.org/aip/apl/article-pdf/doi/10.1063/1.4972183/14489033/241101_1_online.pdf. URL: https://doi.org/10.1063/1.4972183.

Louvet, Geoffrey et al. (July 2020). "Co-sputtered Pr3-doped Ga-Ge-Sb-Se active waveguides for mid-infrared operation". In: *Opt. Express* 28.15, pp. 22511–22523. DOI: 10.1364/OE.398434. URL: https://opg.optica.org/oe/abstract.cfm?URI=oe-28-15-22511.

Ma, Pan et al. (Dec. 2013). "Low-loss chalcogenide waveguides for chemical sensing in the mid-infrared". In: *Opt. Express* 21.24, pp. 29927–29937. DOI: 10.1364/OE.21.029927. URL: https://opg.optica.org/oe/abstract.cfm?URI=oe-21-24-29927.

Maese-Novo, A. et al. (Mar. 2013). "Wavelength independent multimode interference coupler". In: *Opt. Express* 21.6, pp. 7033–7040. DOI: 10.1364/OE.21.007033. URL: https://opg.optica.org/oe/abstract.cfm?URI=oe-21-6-7033.

Mashanovich, Goran Z. et al. (2017). "Germanium Mid-Infrared Photonic Devices". In: *Journal of Lightwave Technology* 35.4, pp. 624–630. DOI: 10.1109/JLT.2016.2632301.

Miller, Steven A. et al. (July 2017). "Low-loss silicon platform for broadband mid-infrared photonics". In: *Optica* 4.7, pp. 707–712. DOI: 10.1364/OPTICA.4.000707. URL: https://opg.optica.org/optica/abstract.cfm?URI=optica-4-7-707.

Optics, Ansys (2023a). *Finite Difference Time Domain (FDTD) solver introduction.* URL: https://optics.ansys.com/hc/en-us/articles/360034914633-FDTD-solver (visited on 06/19/2023).

— (2023b). *MODE - 2.5D varFDTD solver introduction.* URL: https://optics.ansys.com/hc/en-us/articles/360034917213-MODE-2-5D-varFDTD-solver-introduction- (visited on 06/19/2023).

Optics, Ansys (2023c). *MODE- Finite Difference Eigenmode (FDE) solver introduction*. URL: https://optics.ansys.com/hc/en-us/articles/360034917233-MODE-Finite-Difference-Eigenmode-FDE-solver-introduction (visited on 06/19/2023).

— (2023d). *MODE- Finite Difference Eigenmode (FDE) solver introduction*. URL: https://optics.ansys.com/hc/en-us/articles/360034382694-Symmetric-and-anti-symmetric-BCs-in-FDTD-and-MODE (visited on 06/19/2023).

Penades, J. Soler et al. (Oct. 2016). "Suspended silicon mid-infrared waveguide devices with subwavelength grating metamaterial cladding". In: *Opt. Express* 24.20, pp. 22908–22916. DOI: 10.1364/OE.24.022908. URL: https://opg.optica.org/oe/abstract.cfm?URI=oe-24-20-22908.

Penadés, J. Soler et al. (Feb. 2018). "Suspended silicon waveguides for long-wave infrared wavelengths". In: *Opt. Lett.* 43.4, pp. 795–798. DOI: 10.1364/OL.43.000795. URL: https://opg.optica.org/ol/abstract.cfm?URI=ol-43-4-795.

Penadés, Jordi Soler et al. (2015). "Low-Loss Mid-Infrared SOI Slot Waveguides". In: *IEEE Photonics Technology Letters* 27.11, pp. 1197–1199. DOI: 10.1109/LPT.2015.2414791.

Raghunathan, Varun et al. (Oct. 2007). "Demonstration of a Mid-infrared silicon Raman amplifier". In: *Opt. Express* 15.22, pp. 14355–14362. DOI: 10.1364/OE.15.014355. URL: https://opg.optica.org/oe/abstract.cfm?URI=oe-15-22-14355.

Rytov, S (1956). "Electromagnetic properties of a finely stratified medium". In: *Soviet Physics JEPT* 2, pp. 466–475.

Seddon, A.B. (1995). "Chalcogenide glasses: a review of their preparation, properties, and applications". In: *Journal of Non-Crystalline Solids* 184. Non-oxide Glasses, pp. 44–50. ISSN: 0022-3093. DOI: https://doi.org/10.1016/0022-3093(94)00686-5. URL: https://www.sciencedirect.com/science/article/pii/0022309394006865.

Serna, Samuel et al. (Oct. 2019). "Engineering third-order optical nonlinearities in hybrid chalcogenide-on-silicon platform". In: *Opt. Lett.* 44.20, pp. 5009–5012. DOI: 10.1364/OL.44.005009. URL: https://opg.optica.org/ol/abstract.cfm?URI=ol-44-20-5009.

Skryabin, D. V. and A. V. Gorbach (2010). "Theory of supercontinuum and interaction of solitons with dispersive waves". In: *Supercontinuum Generation in Optical Fibers*. Ed. by J. M. Dudley and J. R.Editors Taylor. Cambridge University Press, pp. 178–198. DOI: 10.1017/CBO9780511750465.010.

Spott, Alexander et al. (2017). "Heterogeneous Integration for Mid-infrared Silicon Photonics". In: *IEEE Journal of Selected Topics in Quantum Electronics* 23.6, pp. 1–10. DOI: 10.1109/JSTQE.2017.2697723.

Thi-Thuy, Dinh Duong (2022). "Subwavelength silicon photonic nanostructures for applications in the near IR and mid-IR." PhD thesis. Universite Paris-Saclay.

Wang, Yun et al. (2016). "Compact Broadband Directional Couplers Using Subwavelength Gratings". In: *IEEE Photonics Journal* 8.3, pp. 1–8. DOI: 10.1109/JPHOT.2016.2574335.

Wei, Junxiong et al. (Nov. 2020). "Supercontinuum Generation Assisted by Wave Trapping in Dispersion-Managed Integrated Silicon Waveguides". In: *Phys. Rev. Appl.* 14 (5), p. 054045. DOI: 10.1103/PhysRevApplied.14.054045. URL: https://link.aps.org/doi/10.1103/PhysRevApplied.14.054045.

Worhoff, Kerstin et al. (2009). "Reliable Low-Cost Fabrication of Low-Loss Al_2O_3:Er^{3+} Waveguides With 5.4-dB Optical Gain". In: *IEEE Journal of Quantum Electronics* 45.5, pp. 454–461. DOI: 10.1109/JQE.2009.2013365.

Yao, Yu, Anthony J. Hoffman, and Claire F. Gmachl (July 2012). "Mid-infrared quantum cascade lasers". In: *Nature Photonics* 6.7, pp. 432–439. ISSN: 1749-4893. DOI: 10.1038/nphoton.2012.143. URL: https://doi.org/10.1038/nphoton.2012.143.

Yu, Mengjie et al. (Aug. 2016). "Mode-locked mid-infrared frequency combs in a silicon microresonator". In: *Optica* 3.8, pp. 854–860. DOI: 10.1364/OPTICA.3.000854. URL: https://opg.optica.org/optica/abstract.cfm?URI=optica-3-8-854.

Yu, Yi et al. (Mar. 2016). "Experimental demonstration of linearly polarized supercontinuum generation in a chalcogenide rib waveguide". In: *Opt. Lett.* 41.5, pp. 958–961. DOI: 10.1364/OL.41.000958. URL: https://opg.optica.org/ol/abstract.cfm?URI=ol-41-5-958.

Zhou, Yiyin et al. (Aug. 2020). "Electrically injected GeSn lasers on Si operating up to 100 K". In: *Optica* 7.8, pp. 924–928. DOI: 10.1364/OPTICA.395687. URL: https://opg.optica.org/optica/abstract.cfm?URI=optica-7-8-924.

APPENDIX A. Supercontinuum codes

```
function [Z, AT, AW, W] = gnlse_mod(T, A, w0, gamma, betas,beta0,beta1, ...
                                loss, fr, RT, flength, nsaves)
% Propagate an optical field using the generalised NLSE
% Written by J.C. Travers, M.H. Frosz and J.M. Dudley (2009)
% Updates to this code are available at www.scgbook.info

n = length(T); dT = T(2)-T(1); % grid parameters
V = 2*pi*(-n/2:n/2-1)'/(n*dT); % frequency grid
alpha = log(10.^(loss/10));    % attenuation coefficient

B =beta0+beta1;
for i = 1:length(betas)        % Taylor expansion of betas
  B = B + betas(i)/factorial(i+1).*V.^(i+1);
end
L = 1i*B - alpha/2;            % linear operator

if abs(w0) > eps               % if w0>0 then include shock
    gamma = gamma/w0;
    W = V + w0;                % for shock W is true freq
else
    W = 1;                     % set W to 1 when no shock
end

RW = n*ifft(fftshift(RT.'));   % frequency domain Raman
L = fftshift(L); W = fftshift(W); % shift to fft space

% === define function to return the RHS of Eq. (3.13)
function R = rhs(z, AW)
  AT = fft(AW.*exp(L*z));          % time domain field
  IT = abs(AT).^2;                 % time domain intensity
  if (length(RT) == 1) || (abs(fr) < eps) % no Raman case
    M = ifft(AT.*IT);              % response function
  else
    RS = dT*fr*fft(ifft(IT).*RW); % Raman convolution
    M = ifft(AT.*((1-fr).*IT + RS));% response function
  end
  R = 1i*gamma*W.*M.*exp(-L*z);    % full RHS of Eq. (3.13)
end

% === define function to print ODE integrator status
function status = report(z, y, flag) %
  status = 0;
  if isempty(flag)
    fprintf('%05.1f %% complete\n', z/flength*100);
  end
```

```
end

% === setup and run the ODE integrator
Z = linspace(0, flength, nsaves);  % select output z points
% === set error control options
options = odeset('RelTol', 1e-5, 'AbsTol', 1e-12, ...
                 'NormControl', 'on', ...
                 'OutputFcn', @report);
[Z, AW] = ode45(@rhs, Z, ifft(A), options); % run integrator

% === process output of integrator
AT = zeros(size(AW(1,:)));
for i = 1:length(AW(:,1))
  AW(i,:) = AW(i,:).*exp(L.'*Z(i)); % change variables
  AT(i,:) = fft(AW(i,:));           % time domain output
  AW(i,:) = fftshift(AW(i,:)).*dT*n;  % scale
end

W = V + w0; % the absolute frequency grid
end
```

Program 1 *Solver generalized nonlinear Schrodinger equation*

```
%% Modified code fot supercontinuum generation sim %%
% WC_30_DC_50

%% Load data
%[Wavelenght, Omega(rad),Beta0(1/m),Beta1(s/m),Beta2(s^2/m) neff,Aeff(m^2),
%ng, D(ps/nm*km)]


wavelength = 3.534e-6;        % reference wavelength [m]
c = 299792458;               % speed of light [m/s]
w0 = (2*pi*c)/wavelength;    % reference frequency [Hz]

n = 2^13;                    % number of grid points
twidth = 12.5e-12;           % width of time window [s]
dt = twidth/n;
T = (-n/2:n/2 - 1).*dt; % time grid

% === input pulse

power = 1000;               % peak power of input [W]
t0 = 220e-15;               % duration of input [s]
A = sqrt(power)*(sech(T/t0)).^2; % input field [W^(1/2)]

% === fibre parameters
flength = 4e-3;              % fibre length [m]
```

```
n2=2.5e-18;
Aeff=1.714830620827234e-12;

beta0=  5233437.162744169;
beta1=1.213274122078790e-08;
betas= -7.770844291581464e-25;
% betas = [beta2] in units [s^2/m, s^3/m ...]
gamma = ((w0*n2)/(Aeff*c));               % nonlinear coefficient [1/W/m]
loss =0 ;                    % loss [dB/m]

% === Raman response
fr = 0;                   % fractional Raman contribution
tau1 = 0.0122e-12; tau2 = 0.032e-12;
RT = (tau1^2+tau2^2)/tau1/tau2^2*exp(-T/tau2).*sin(T/tau1);
RT(T<0) = 0;                 % heaviside step function

% === simulation parameters
nsaves = 300;     % number of length steps to save field at

% propagate field
[Z, AT, AW, W] = gnlse_mod(T, A, w0, gamma, betas,beta0,beta1, loss, ...
                        fr, RT, flength, nsaves);

% === plot output
figure();

%Distance vs Wavelength
WL = 2*pi*c./W; iis = (WL>1e-6 & WL<8e-6); % wavelength grid
lIW = 10*log10(abs(AW).^2 .* 2*pi*c./WL'.^2); % log scale spectral intensity
mlIW = max(max(lIW));        % max value, for scaling plot
subplot(1,2,1);
pcolor(WL(iis).*1e9, Z, lIW(:,iis)); % plot as pseudocolor map
colormap('jet')
caxis([mlIW-40.0, mlIW]);  xlim([1000,8000]); shading interp;
xlabel('Wavelength [nm]'); ylabel('Distance [m]');


lIT = 10*log10(abs(AT).^2); % log scale temporal intensity
mlIT = max(max(lIT));        % max value, for scaling plot
subplot(1,2,2);
pcolor(T.*1e12, Z, lIT);     % plot as pseudocolor map
caxis([mlIT-40.0, mlIT]);  xlim([-4,4]); shading interp;
xlabel('Time [ps]'); ylabel('Distance [m]');
```

Program 2 *Supercontinuum generation*